HHS Public Access

Author manuscript

Mol Cell. Author manuscript; available in PMC 2021 November 19.

Published in final edited form as:

Mol Cell. 2020 November 19; 80(4): 633–647.e7. doi:10.1016/j.molcel.2020.10.026.

Stabilization of ERK-Phosphorylated METTL3 by USP5 Increases m^{6}A Methylation

Hui-Lung Sun[1,2,9], **Allen C. Zhu**[1,2,3,9], **Yawei Gao**[4], **Hideki Terajima**[1,2], **Qili Fei**[1,2], **Shun Liu**[1,2], **Linda Zhang**[1,2], **Zijie Zhang**[1,2], **Bryan T. Harada**[1,2], **Yu-Ying He**[5], **Marc B. Bissonnette**[6], **Mien-Chie Hung**[7], **Chuan He**[1,2,8,10,*]

[1]Department of Chemistry and Institute for Biophysical Dynamics, The University of Chicago, Chicago, IL 60637 USA.

[2]Howard Hughes Medical Institute, The University of Chicago, Chicago, IL 60637, USA.

[3]Medical Scientist Training Program, The University of Chicago, Chicago, IL 60637, USA.

[4]Clinical and Translational Research Center of Shanghai First Maternity and Infant Hospital, Shanghai Key Laboratory of Signaling and Disease Research, School of Life Sciences and Technology, Tongji University, Shanghai 200092, China.

[5]Department of Medicine, Section of Dermatology, University of Chicago, Chicago, IL, 60637, USA.

[6]Department of Medicine, The University of Chicago, Chicago, IL 60637, USA.

[7]China Medical University, Taichung 404, Taiwan.

[8]Department of Biochemistry and Molecular Biology, The University of Chicago, Chicago, IL, USA.

[9]These authors contributed equally.

[10]Lead Contact

Summary

N^6-methyladenosine (m^{6}A) is the most abundant mRNA modification, which is installed by the METTL3-METTL14-WTAP methyltransferase complex. Although the importance of m^{6}A methylation in mRNA dynamics has been well-documented recently, the regulation of m^{6}A machinery remains obscure. Through a genome-wide CRISPR screen, we identify the ERK

*Correspondence: chuanhe@uchicago.edu (C.H.).

Author Contributions

H.S. and A.Z. carried out most of the experiments, assembled the figures, and wrote the manuscript; A.Z. analyzed CRISPR screen, RNA-seq, and m^{6}A-seq data; Y.G. helped with mESCs culture; H.T. helped with the CRISPR screen; Q.F. helped analyze CRISPR screen data; S.L., L.Z., Z.Z., and B.T.H. provided suggestions for experimental design, manuscript writing, or bioinformatic analysis; M.B.B., M.H., and Y.Y.H. provided suggestions for cancer-related experiments and cell lines; and C.H. supervised the project.

Declaration of Interests

C.H. is a scientific founder and a member of the scientific advisory board of Accent Therapeutics, Inc.

pathway and USP5 as positive regulators of the m^{6}A pathway. We find that ERK phosphorylates METTL3 at S43/S50/S525 and WTAP at S306/S341, followed by deubiquitination by USP5, resulting in stabilization of the m^{6}A methyltransferase complex. Lack of METTL3/WTAP phosphorylation reduces decay of m^{6}A-labeled pluripotent factors and traps mouse embryonic stem cells in the pluripotent state. The same phosphorylation can also be found in ERK-activated human cancer cells and contribute to tumorigenesis. Overall, our study reveals an unrecognized function of ERK in regulating m^{6}A methylation.

Graphical Abstract

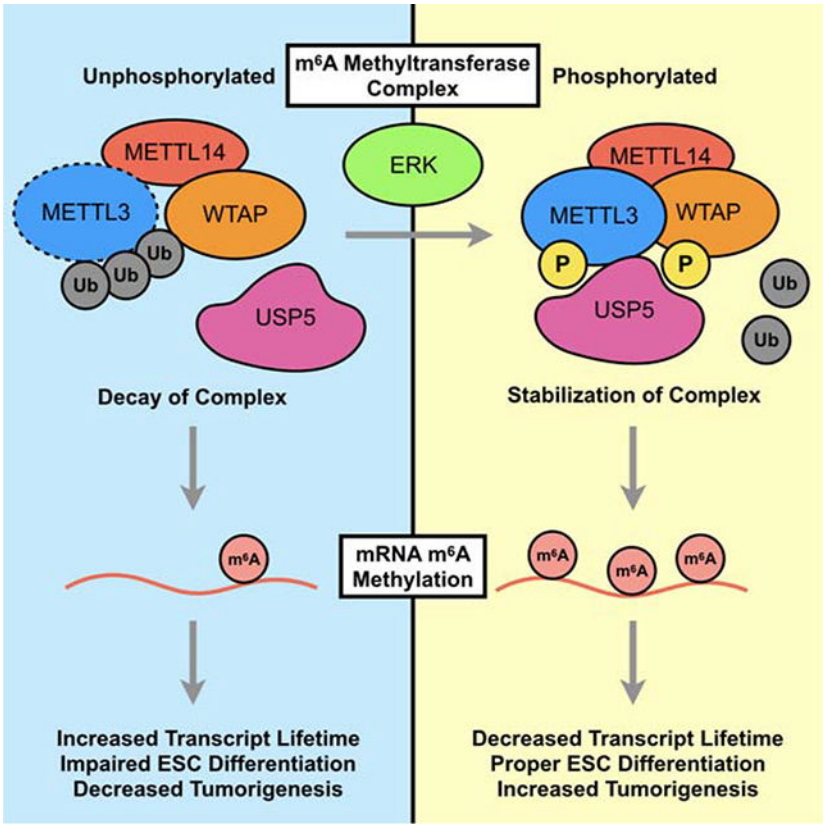

eTOC Blurb

Sun et al. demonstrate that activation of the ERK pathway promotes m^{6}A methylation by phosphorylation of METTL3 and WTAP. Phosphorylation of METTL3 increases interaction with USP5, thereby decreasing ubiquitination to stabilize the m^{6}A methyltransferase complex. Activation of the ERK-METTL3/WTAP signaling axis promotes stem cell differentiation and tumorigenesis.

Keywords

ERK; METTL3; WTAP; m^{6}A; USP5

Introduction

Recent studies have shown that messenger RNA (mRNA) modifications play a critical role in regulating biological and pathological processes (Frye et al., 2018). Among over 150 known RNA modifications, N^6-methyladenosine (m^6A) is an evolutionarily conserved and the most abundant internal mRNA modification in eukaryotic mRNA. m^6A is reversibly, site-selectively installed on mRNA transcripts by "writers," with a portion that can be removed by "erasers". The m^6A methylation is mediated by a core complex of three components: METTL3, METL14, and WTAP (Liu et al., 2014). The crystal structure of the METTL3 and METTL14 complex suggests that METTL3 is the catalytic component while METTL14 contributes to substrate RNA binding. WTAP, on the other hand, recruits METTL3 and METTL14 to nuclear speckles (Ping et al., 2014; Wang et al., 2014b). Meanwhile, "eraser" proteins FTO and ALKBH5 remove m^6A modification (Jia et al., 2011; Zheng et al., 2013).

Increasing evidence suggests that the m^6A modification is involved in the regulation of RNA splicing, localization, stability, and translation (Shi et al., 2017; Wang et al., 2014a; Wang et al., 2015; Xiao et al., 2016; Zhou et al., 2019). It has been found that m^6A affects numerous physiological and pathological processes. For example, loss of METTL3 in mouse embryonic cells (mESCs) depletes m^6A and increases stability of certain transcripts such as *Nanog* (Batista et al., 2014; Wang et al., 2014b). This impedes decay of pluripotency factors, thereby delaying proper lineage priming and fate transition, leading to early embryo lethality (Geula et al., 2015). Furthermore, METTL3 knockdown is known to induce apoptosis (Dominissini et al., 2012) and METTL3 overexpression can promote tumorigenesis in multiple cancer types (Barbieri et al., 2017; Cai et al., 2018; Chen et al., 2018; Cheng et al., 2019; Dahal et al., 2019; Hua et al., 2018; Li et al., 2019; Lin et al., 2016; Liu et al., 2019; Miao et al., 2019; Taketo et al., 2018; Visvanathan et al., 2018; Vu et al., 2017).

The importance of m^6A methylation has been well described, yet gaps in our understanding of how this process is regulated remain. We therefore used a genome-wide CRISPR screen to identify regulators of m^6A methylation. The biological importance of these regulations was further studied in mESCs and relevant cancer cells.

Results:

ERK Activation Promotes mRNA m^6A Methylation

To identify regulators of m^6A RNA methylation, we employed a circular RNA GFP reporter containing a consensus GGACU motif in HeLa cells. The GFP pre-mRNA transcript is assembled by back-splicing to generate a circular RNA that joins two exon fragments of GFP, as depicted in Figure 1A. m^6A methylation of the GGACU motifs on the circular RNA can drive translation initiation of the GFP transcript, producing GFP fluorescence signal. Consequently, the GFP signal from this circular RNA reporter can be used as a readout of m^6A methylation. Indeed, consistent with a previous report (Yang et al., 2017), circRNA containing GGACT was translated into GFP, whereas mutation to GGTCT reduced GFP levels. Co-expression of METTL3 increased GFP expression from the GGACT reporter but not the GGTCT control (Figure S1A). Furthermore, signal from the GGACT reporter was

decreased by catalytic mutant D395A METTL3, as well as siMETTL3, siMETTL14, and siWTAP, but was increased by siFTO and siALKBH5 (Figure S1A).

Next, we performed a CRISPR knockout-based genomic screen targeting 19,050 genes and 1,864 miRNA (Joung et al., 2017). Combining a CRISPR knockout library with a circular RNA m^{6}A-GFP reporter allowed us to screen for possible regulators of m^{6}A methylation (Figure 1B). Knockout of genes that promote or suppress m^{6}A methylation would decrease or increase translation of the GFP transcript, respectively. Cells with the top and bottom 5% of GFP expression were therefore collected, followed by high-throughput sequencing in order to identify negative and positive regulators of m^{6}A methylation, respectively. We compared the genes that were enriched in the low-GFP-expressing and the high-GFP-expression populations (Table S1). As expected, knockout of METTL3 led to low GFP signal in the screen (Figure 1C). Interestingly, pathway enrichment analysis of the gRNAs in low-GFP-expressing cells identified genes involved in the RAS and MAPK signaling pathways (Figure 1C–D and Table S2). Several hits which are known to activate ERK, including SHC1, CDC42, MAP3K1, PTPN11, and GRB2, decreased GFP signal from the GGACT reporter significantly more than the control GGTCT reporter (Figure S1B).

To determine how the RAS/MAPK pathway affects m^{6}A methylation, we investigated the status of the m^{6}A methyltransferase complex during MAPK pathway activation. A phos-tag gel (Kinoshita et al., 2006) revealed that constitutively active MEK S218D/S222D, BRAF V600E, or HER2 V659E, increased the phosphorylation-dependent mobility shift of METTL3 and WTAP, but not METTL14 (Figure S1C). We further co-transfected a panel of 13 oncogenic kinases, including ATM, ATR, IKK-α, IKK-β, IKK-ε, AKT, GSK-3β, mTOR, MEK, CDC2, FAK, EGFR, and HER2 with METTL3 in 293T cells. As shown in Figure S1D, MEK and HER2, which activate ERK, induced the most significant phosphorylation-dependent mobility shift of METTL3. We also employed *NANOG* 3’ UTR, which contains three m^{6}A consensus RRACT motif sites that mediate the methylation-dependent decay of *NANOG* (Zhang et al., 2016), as a readout of the cellular m^{6}A methylation activity. Mutation of the adenosine residue (AAACT to AATCT, and GGACT to GGTCT) resulted in increased luciferase activity, suggesting that the mutation prevented methylation and thereby increased the stability of the luciferase-*NANOG* 3’-UTR fusion mRNA. We noticed that overexpression of the m^{6}A methyltransferase complex (METTL3-METTL14-WTAP) decreased wild type RRACT but not mutant RRTCT reporter expression. Overexpression of the ERK activators alone decreased WT *NANOG* 3’UTR reporter expression, and the effect was enhanced with the m^{6}A methyltransferase complex (Figure S1E). Together, our results show that the activation of MAPK pathway promotes mRNA m^{6}A methylation.

ERK Phosphorylates METTL3 and WTAP

To determine how ERK activates m^{6}A methylation, we first tested whether ERK interacts with the mRNA m^{6}A methyltransferase complex. Co-immunoprecipitation showed that METTL3 associates with ERK1 and ERK2 upon BRAF transfection (Figure S2A). Considering that ERK1 and ERK2 are highly similar and possess identical substrate specificity *in vitro*, we focused on ERK2 hereafter because ERK2 expression exceeds ERK1 in most cells. The interaction between ERK2 and WTAP was also observed after RAF

activation (Figure S2B). The interaction of endogenous ERK2 with METTL3 and WTAP was observed in A375 cells, a human melanoma cell line with constitutively active ERK due to a BRAF V600E mutation (Fig 2A). After MEK stimulation, activated ERK translocates into the cell nucleus to activate nuclear substrates, or forms a dimer to activate cytoplasmic substrates (Casar et al., 2009). As shown in Figure S2C, ERK activated by BRAF co-localizes with METTL3 and WTAP in the nucleus, suggesting that METTL3 complex could be a nuclear substrate of ERK.

ERK displays a specificity for phosphorylation at the serine/threonine-proline (S/T-P) motif. Since the S/T-P motif is found in many proteins, ERK either uses a common docking domain (Matsuoka et al.) to bind to a D domain ($K/R_{\mathbf{0-2}}$-X_{1-6}-φ-X-φ) or uses the F-site recruitment site (FRS) to bind to the F-site (FX-F/Y-P) (Roskoski, 2012). Analysis using the Eukaryotic Linear Motif database (http://elm.eu.org) revealed residues 415–421 in METTL3 and residues 71–77 in WTAP as potentially conserved D domains (Figure 2B). We found that a CD mutant (321N) form of ERK2, but not an FRS mutant (263A) form, abolished its interaction with METTL3 and WTAP (Figure 2C). Mutational analysis of the putative D domain residues of METTL3 and WTAP abolished the interaction. Co-IP showed that ERK2 only binds to the myc-tagged domain where the D-domain is located (Figure S2D). These results support the interaction of ERK with METTL3 and WTAP.

Given the physical interaction between ERK and METTL3, and that calf intestinal alkaline phosphatase can eliminate the mobility shift induced by ERK (Figure S2E), we examined whether METTL3 is a physiological substrate of ERK. *In vitro* kinase assay suggests that ERK directly phosphorylates METTL3 (Figure S2F). We noticed that p38 and JNK, but not ERK5, phosphorylate METTL3, although not as strongly as ERK2. Mass spectrometry analysis showed that ERK phosphorylates METTL3 at three highly conserved residues S43, S50, and S525 (Figure 2D–E). Mutational analysis further confirmed these three sites as main ERK phosphorylation sites (Figure 2F). There is no available structure for WTAP, and published studies of the METTL3 structure focus on the SAM-binding and methyltransferase domains, which cannot provide information for S43 and S50. However, we noticed that S525 lies on the same face and close to the D Domain of METTL3 (Fig S2H). This suggests that the phosphorylation occurs near the ERK binding region.

To investigate METTL3 phosphorylation by ERK inside cells, we raised a polyclonal antibody that targets S43-phosphorylated METTL3. This antibody recognizes S43-phosphorylated METTL3 but not a mutant form of METTL3, 3A METTL3, in which all three phosphorylation serine sites are replaced with alanine (Figure S2F). This P-S43 antibody was then used as a tool to monitor METTL3 phosphorylation. The endogenous METTL3 phosphorylation can be detected in A375 (BRAF-V600E mutant) and HCT116 (K-Ras-G12D mutant) and abrogated by MEK inhibitor treatment for 1 hour (PD0325901 or trametinib) (Fig S2I–J). Although this antibody is not suitable for immunoprecipitation (data not shown), phos-tag gels suggested about 80% of endogenous METTL3 was phosphorylated in A375 and HCT116 and decreased to 40% upon addition of MEK inhibitors.

To determine the phosphorylation sites of WTAP, we examined whether mutations of the S/T-P motif affect the ERK-induced phosphorylation. Among the three S/T-P motifs in human WTAP (Figure 2G), we found that S306 and S341 are the main ERK phosphorylation sites of human WTAP (Figure 2H). We noticed that S306 is not conserved in mouse and rat WTAP orthologs; however, there is a unique S/T-P motif at T298 in mouse and rat WTAP, which can also be phosphorylated by ERK (Figure S2K). In conclusion, we show that ERK interacts with and phosphorylates METTL3 and WTAP.

USP5 is Required for ERK-Mediated METTL3 Stabilization

Next, we investigated how ERK-induced phosphorylation increases RNA m^6A methyltransferase complex activity. We noticed that ERK activation increased wild-type (WT) but not 3A METTL3 expression (Figure 2F), and that WT METTL3 stable transfectants maintained consistently higher expression levels than those of 3A METTL3 in both mouse ESCs (mESCs) and human A375 cells. (Figure 3A). This observation suggested a model in which METTL3 phosphorylation by ERK stabilizes the protein, which could explain the higher METTL3 protein level and elevated m^6A methylation activity observed with ERK activation. We then investigated whether ERK activation could affect METTL3 stability and found that inhibition of ERK by PD0325901 increased its ubiquitination at 8-hour treatment (Figure S3A). Furthermore, the degradation of METTL3 induced by inhibition of ERK activity was restored by addition of a proteasome inhibitor MG132 (Figure S3B). The ubiquitination level of 3A METTL3 was also higher than that of WT METTL3 (Figure 3B). To assess more directly the effects of ERK on METTL3 stability, cycloheximide was used to suppress protein synthesis and the degradation of METTL3 protein was monitored. As shown in Figure 3C, ERK activation increased the stability of WT but not non-phosphorylatable 3A METTL3; meanwhile, phospho-mimetic 3E METTL3 showed an increase in stability compared to WT METTL3.

Since METTL14 is known to stabilize METTL3 (Wang et al., 2016), we investigated whether phosphorylation of METTL3 by ERK affects METTL3-METTL14 complex formation. The interaction between METTL3 and METTL14 was not obviously affected by ERK inhibition treatment for 1 hour (Figure S3C). Moreover, 3A METTL3 also interacts with METTL14 normally (Figure S3D). Interestingly, we noticed that ERK activation increased the interaction between METTL3 and WTAP, which became weaker with 3A METTL3 and was further attenuated with non-phosphorylatable WTAP S306A/S341A (2A) (Figure S3D). It has been shown that WTAP depletion does not affect METTL3 complex stability, but rather reduces nuclear localization of METTL3 (Kobayashi et al., 2018; Ping et al., 2014). Consistent with previous reports, knockdown of WTAP decreased nuclear METTL3 (Figure S3E). Considering the interaction between METTL3 and WTAP was attenuated by non-phosphorylatable mutant forms, cellular fractionation and immunostaining was used to examine METTL3. As shown in Figure S3F–G, nuclear METTL3 was markedly reduced in cells expressing 3A METTL3 and 2A WTAP.

To gain further insight into how ERK phosphorylation decreases METTL3 ubiquitination, we examined whether any ubiquitin ligases or deubiquitinases were identified in our CRISPR-based genomic screen. Since the top hits identify regulators of GGACT reporter

m^{6}A methylation rather than just METTL3, not all hits—namely, USP43, USP15, or USP7 (Table S1, top 1000 sgRNAs)—affected METTL3 expression level (Figure S4A). However, we found knockdown of USP5 and USP1 (Rank 2845 and 2339) decreased METTL3 in A375 (Figure S4B). Commercially available USP1 inhibitor SJB3–019A and USP5 inhibitor EOAI3402143 (EOAI) also decreased METTL3 (Figure S4C). Considering USP5 is implicated in a wide range of pathological processes and had the most pronounced effect on METTL3, we chose to further investigate it.

We first investigated whether phosphorylation of METTL3 in the presence of activated BRAF affects the METTL3-USP5 interaction. We noticed that ERK activation increased the interaction between METTL3 and USP5, which became weaker with phospho-defective mutant S43A, S50A, S525A, and fully attenuated when all three sites were mutated (Figure 3D). We also noticed that 3E METTL3 binds to USP5 more strongly. Interestingly, BRAF expression further promoted 3E METTL3-USP5 interaction and increased its expression. This suggests that BRAF may also affect USP5 activity. It has been demonstrated that USP5 activity was increased in cells expressing BRAF V600E (Potu et al., 2014). We further find that ERK activation by BRAF promoted USP5 translocation into the nucleus to colocalize with METTL3 (Figure S4D). USP5 is a large protein composed of five specific domains, including the cryptic ZnF domain, ZnF domain, C-box domain, UBA1/UBA2 domain, and H-box domain. To define which domain was critical for the action of USP5 on METTL3, constructs of these domains were co-transfected with METTL3. The IP assay suggested that METTL3 binds more strongly to the cryptic ZnF domain compared to the C-box domain and H-box domain (Figure S4E). On the other hand, USP5 binds to the methyltransferase domain of METTL3 (Figure S4F). Reciprocal IP confirmed the endogenous METTL3-USP5 interaction, which was inhibited by MEK inhibitor (Figure S4G). Lastly, ERK-phosphorylated or phosphomimetic 3E METTL3 displayed greater stability upon USP5 inhibitor EOAI treatment (Figure S4H). Taken together, these results suggest that ERK activation translocates USP5 to the cell nucleus, which interacts with phosphorylated METTL3 to promote its stability.

Because USP5 is an enzyme that could prevent protein ubiquitination, we further examined whether USP5 stabilizes METTL3 through deubiquitination (Figure 3E). Overexpression of wild-type but not catalytically dead C335A USP5 decreased ubiquitination and stabilized METTL3. Furthermore, *in vitro* addition of USP5 reduced EOAI-induced METTL3 ubiquitination (Figure S4I), suggesting that METTL3 is a direct substrate of USP5. To identify ubiquitin ligases that contribute to USP5 inhibition-induced degradation of METTL3, we searched consensus motif and physical association databases, as well as our CRISPR-based genomic screen. METTL3 contains an SPOP-binding consensus motif and COP1-binding destruction motif (http://elm.eu.org). It also interacts with TRIM28, HUWE1, and UBR5 (https://thebiogrid.org), and may be ubiquitinated by SMURF1 (http://ubibrowser.ncpsb.org). Finally, we identified FBXW8, FBXW12, SPOPL, TRIM2, and ANAPC1 as negative regulators of m^{6}A methylation from our CRISPR screen. To find ubiquitin ligases involved in METTL3 degradation, A375 cells with USP5 knockdown were further transfected with siRNA targeting ubiquitin ligases. Knockdown of SPOP, TRIM28, or ANAPC1 partially abolished USP5 inhibition-mediated METTL3 degradation (Figure 3F). Because SPOP is a well-known tumor suppressor and localizes to nuclear speckles

(where the m^{6}A methyltransferase localizes), we tested an SPOP inhibitor, SPOP-IN-6b, which was able to partially reverse EOAI-induced ubiquitination and degradation of METTL3 (Figure S4J–K). Lastly, we were interested in what type of ubiquitin linkages that the USP5 inhibition induced. USP5 has been shown to cleave multiple types of polyubiquitin linkage, including K6, K11, K29, K48 and K63 (Avvakumov et al., 2012; Raasi et al., 2005). We observed K11, K48 and K63-linked polyubiquitination on METTL3 after USP5 knockdown. Furthermore, knockdown of ANAPC1 and SPOP decreased K11 and K48 ubiquitination, respectively (Figure S4L). In summary, these results suggest that USP5 stabilizes METTL3 through deubiquitination.

Phosphorylation of METTL3/WTAP by ERK Facilitates Resolution of Pluripotency

Autocrine FGF4 is reported to be the major stimulus for ERK signaling in mESCs. Interference with FGFR or ERK activity impeded the ability of mESCs to undergo differentiation and retain expression of pluripotency factors including *Nanog*. We observed that p-43 METTL3 phosphorylation was enhanced by FGF4 and reduced by MEK inhibitor PD0325901 or FGFR1 inhibitor PD173074 (Figure S5A). Because both ERK activation and METTL3 expression have been reported to be required for mESCs to exit the pluripotent state upon differentiation, we further investigated whether phosphorylation of METTL3/WTAP affects mESCs fate. We introduced TetOn-shWTAP into METTL3-KO mESCs to tune endogenous WTAP expression. Cells were then transduced with WT or a phospho-inactive mutant of CuO-METTL3-T2A-WTAP constructs. With 50 μg/ml cumate, the expression level of exogenous R-WT METTL3 is comparable to that of endogenous METTL3 and we noticed that 3A METTL3 expression is consistently lower than that of WT (Figure S5B). Quantification of m^{6}A by LC-MS/MS showed a synergistic reduction of 3A METTL3 and 2A WTAP (Figure 4A). We then examined whether pluripotency of mESCs expressing R-3A2A was affected. R-3A2A mESCs exhibited higher stage specific embryonic antigen 1 (SSEA-1) expression (Figure S5C) and increased proliferation (Figure 4B). These observations support the notion that loss of METTL3 and WTAP phosphorylation trap mESCs in the pluripotent state.

Mettl3-deficient mESCs fail to exit pluripotency despite differentiation cues, likely because loss of m^{6}A impedes the degradation of pluripotency-promoting transcripts. We subsequently examined reported m^{6}A-methylated pluripotency factor transcripts, including *Nanog*, *Zfp42*, *Klf2*, *Sox2*, and *Lefty1* (Batista et al., 2014; Bertero et al., 2018; Geula et al., 2015). *Pou5f1*, which does not harbor any m^{6}A modification, was also used as a negative control. m^{6}A-RIP-qPCR confirmed decreased m^{6}A (Figure 4C) and RT-qPCR indicated upregulation (Figure 4D) of these m^{6}A-labeled pluripotency transcripts in R-3A2A mESCs. Furthermore, after transcription arrest by actinomycin D treatment, these transcripts showed delayed turnover in R-3A2A (Figure S5D). These findings suggest that METTL3 phosphorylation controls the level of critical pluripotency regulators. Considering ERK activation is the primary stimulus for mESCs to exit self-renewal and acquire competence of differentiation (Kunath et al., 2007), we then compared the capacity for differentiation by transferring mESCs to differentiation media for embryoid bodies (EBs). R-3A2A mESCs generated smaller EB spheres (Figure S5E), failed to repress pluripotent genes, and adequately up-regulated developmental markers (Figure 4E). Lastly, because ERK activation

controls the transition from the primitive ectoderm-like cell state to a neural progenitor cell state, we tested whether METTL3 phosphorylation could affect differentiation towards a neural lineage. As shown in Figure S5F, even upon induction of differentiation, R-3A2A mESCs continued to express *Nanog* and failed to upregulate primary neural markers *Sox1* and *Nestin*. These results support the notion that ERK-dependent phosphorylation of METTL3 and WTAP promotes mESC differentiation.

Transcripts Affected by Phosphorylation of Methyltransferase Complex in mESCs

To gain further insight into how the phosphorylation of the m^{6}A methyltransferase complex affects the m^{6}A-modified transcripts, we mapped the m^{6}A methylome in mESCs. Comparison of the R-WT with R-3A2A mESCs revealed a global loss of methylation sites (Figure 5A). Consistent with previous m^{6}A-seq results (Dominissini et al., 2012; Meyer et al., 2012), the m^{6}A peaks identified are enriched near the start and stop codons and were characterized by the canonical GGACU motifs (Figure S6A–B). Using our in-house R-package "MeRIPtools," which tests for m^{6}A-IP enrichment using a binomial-distribution-based model, we found 7,591 m^{6}A peaks that exhibited a significant decrease in the R-3A2A cells compared to the R-WT cells (Figure 5B, Table S3), such as modification sites in *Nanog*, *Lefty1*, and *Zfp219* (Figure 5C). The genes showing decreased m^{6}A methylation significantly overlap with those in functional gene sets important for pluripotency, including targets of NANOG and MYC (Figure S6C). The transcripts exhibiting differential methylation were consistent between replicates (Figure S6D). Furthermore, the transcripts showing decreased m^{6}A methylation (Figure 5D) and differential expression (Figure 5E) were enriched for gene ontology (GO) terms related to pluripotency and mRNA processing. Importantly, many of the genes involved in pluripotency showed reduced m^{6}A methylation in R-3A2A when compared with R-WT mESCs (Figure 5F).

To expand our observation of pathways that are enriched when comparing R-WT and R-3A2A mESCs, we performed a functional class scoring approach (gene-set enrichment analysis, GSEA) in addition to GO analysis. GSEA showed enrichment of histone binding proteins (Figure S6E, Table S4). Considering that it has been reported that m^{6}A regulates histone modifications in part by destabilizing mRNA of histone-modifying enzymes (Wang et al., 2018), we used an ELISA kit to compare 21 different Histone H3 modifications. H3K27me3 showed the most dramatic changes (Figure S6F) and we detected reduced m^{6}A peaks in several components of the PRC2 complex mRNA (Figure S6G). These results suggest phosphorylation of the m^{6}A methyltransferase complex decreases H3K27me3 partially by regulating the PRC2 complex.

Phosphorylation of the m^{6}A Methyltransferase Complex May Affect Tumorigenesis

As one of the most frequently mutated signaling pathways in cancer, the RAS/RAF/MEK/ERK signaling cascade has long been viewed as a promising target for cancer therapy (Liu et al., 2018a). Given that phosphorylation of the m^{6}A methyltransferase complex by ERK facilitates resolution of pluripotency in mESCs, we further investigated whether the m^{6}A methyltransferase complex can be similarly regulated in certain cancer cells. Using CancerMine (Lever et al., 2019), a literature-mined resource, we summarized that METTL3 could behave as an oncogene in many cancer types (Figure S7A).

We first examined melanoma due to the high prevalence of constitutively active *BRAF V600E* mutation (50–60%) and clinical success with BRAF and MEK inhibitors (Schadendorf et al., 2018). The m^6A levels on mRNA are higher in MEL-624 and A375 cells, which harbor a *BRAF V600E* mutation (Fig S7B). As expected, the stability of the m^6A methyltransferase complex was reduced in the R-3A2A A375 cells (Figure 6A), which contributed to the overall lower m^6A level on mRNA (Figure 6B). MEK inhibitors PD0325901 and trametinib were found to reduce the protein levels of the m^6A methyltransferase complex at 8 hours (Figure 6C) and the overall mRNA m^6A levels at 48 hours (Figure 6D) in A375 melanoma cells. In addition, these two MEK inhibitors also decreased m^6A methyltransferase complex level in HCT-116 cells, which is a colon cancer line that possesses the most common *KRAS* mutation (G12D) (Figure S7C).

Because knockdown of USP5 increases METTL3 in A375 melanoma cells (Figure S5B), we assessed the potential clinical relevance of USP5. Interestingly, melanoma patients with high USP5 had shorter overall survival (Figure S7D). Two structurally unrelated USP5 inhibitors, EOAI3402143 and vialinin, were employed to evaluate the effect of USP5 on the METTL3 level in melanoma cells. We found that these two USP5 inhibitors increased ubiquitination of METTL3, resulting in decreased METTL3 protein level (Figure 6E and S7E–F). Furthermore, MEK inhibition, R-3A2A, or METTL3-WTAP knockdown can sensitize melanoma and colon cancer cells to USP5 inhibition (Figure 6F and S7G), supporting the connection between USP5 and METTL3.

Lastly, considering that HER2 expression phosphorylates METTL3 and WTAP (Figure S1C and S7H) and m^6A levels are higher in the HER2-overexpressed SKBR3 and BT474 cells (Figure S7I), we investigated whether inhibition of HER2 could affect m^6A methylation. Two HER2 inhibitors, tucatinib and lapatinib, could reduce METTL3 protein level at 8 hours and cellular mRNA m^6A methylation at 48 hours in HER2-positive breast cancer (Figure 6G and 6H). Overall, our data support that ERK-dependent METTL3 stabilization affects cellular mRNA m^6A methylation which could contribute to tumorigenesis. More focused cancer studies are required to assess the effects and scope of such a regulatory mechanism in the future.

Discussion

m^6A RNA methylation plays crucial roles in regulating RNA metabolism. While many studies have shown the importance of METTL3 (Batista et al., 2014; Choe et al., 2018; Geula et al., 2015; Lin et al., 2016; Liu et al., 2018b; Wang et al., 2014b), few have shown how the methyltransferase complex itself is regulated. Here, we identify an ERK-METTL3/WTAP signaling axis that regulates mESCs differentiation and potentially affects tumorigenesis. Initially, we deployed a genome-wide CRISPR screen using an m^6A methylation-dependent GFP reporter. RAS and MAPK pathways were identified as the top pathways in the positive regulation of m^6A methylation. Biochemical studies showed that ERK proteins could phosphorylate METTL3 on S43/S50/S525 and WTAP at S306/S341. We also found that phosphorylation of METTL3 decreases METTL3 ubiquitination through interaction with USP5. These findings explain elevated m^6A levels on mRNA upon ERK

activation. This pathway underlines a previously unrecognized effect of ERK activation through RNA methylation during differentiation of pluripotent mESCs (Figure 7).

Phosphorylation of METTL3 and Potential Effects

Our studies reveal METTL3 phosphorylation by ATM and ATR (Figure S1D). Phosphoproteomic studies of ATM/ATR substrates have previously uncovered that, in response to DNA damage, METTL3 was phosphorylated at residues S350 and T356 in an ATM-dependent manner (Matsuoka et al., 2007). Furthermore, phosphorylation of METTL3 was found to be an early responder to DNA damage (Bennetzen et al., 2010). Considering that m^6A rapidly accumulates at UV-irradiated sites (Xiang et al., 2017) and lack of METTL3 catalytic activity delays DNA repair and Pol κ-mediated response to UV DNA damage, it would be interesting to explore the role of ATM/ATR-induced METTL3 phosphorylation in the future. In addition, *in vitro* kinase assay showed that certain stress-activated MAP kinase, p38 and JNK, can also phosphorylate METTL3. Interestingly, METTL3 has previously been linked to MAPK signaling. In dendritic cells, dental pulp stem cells, or intestinal epithelia, depletion of METTL3 leads to reduced phosphorylation of p38, ERK, and JNK (Feng et al., 2018; Wang et al., 2019; Zong et al., 2019); whereas phosphorylation is increased in osteoblasts and colorectal cancer cells (Deng et al., 2019; Zhang et al., 2019a). Although effects of METTL3 on MAPKs may vary based on cell type, taken together, these data suggest potential feedback loop mechanisms between METTL3 and MAPK pathways.

Our phosphorylation studies estimated the relative levels of phosphorylated and non-phosphorylated METTL3. We noticed that trametinib was more effective than PD0325901 in decreasing the mobility shift of METTL3 in A375 cells, although these two MEK inhibitors inhibited ERK activation and METTL3 S43 phosphorylation equally well (Figure S3H). Trametinib is known to inhibit the proliferation of BRAF V600E cells with lower IC50 than PD0325901, even though they had similar potency against MEK1 *in vitro*. Part of the reason is that trametinib inhibits the CRAF-driven signaling more effectively than PD0325901 (Lito et al., 2014). We observed that CRAF phosphorylates METTL3 and leads to an additional band in the 3A METTL3 mutant, when comparing to MEK and BRAF expression (data not shown). Therefore, we propose that the more potent effect of trametinib could be partially due to CRAF inhibition. Although the RAF family of enzymes are canonically depicted as activators of MEK, they carry out additional functions as well. BRAF is the most potent MEK activator *in vivo*, whereas ARAF and CRAF interact with several other proteins in a MEK-independent manner (Desideri et al., 2015; Leicht et al., 2007). Interestingly, ARAF is also detected in our CRISPR screen (Figure 1C). How ARAF and CRAF affect METTL3 through MEK-independent signaling pathway still needs future investigation.

Ubiquitin Ligases and Ubiquitin Linkages of METTL3

To systemically study the regulation of METTL3 ubiquitination, we plan to construct a reporter encoding both DsRed and EGFP-METTL3, which allows us to use EGFP:DsRED ratio as an indicator of the stability of METTL3 in the future (Yen et al., 2008). CRISPR activation (CRISPRa) and CRISPR inhibition (CRISPRi) screens, which focus on proteostasis, could be used to identify ubiquitin ligases and deubiquitinases for METTL3. In

the current study, we found that SPOP, ANAPC1, and TRIM28 promote degradation of METTL3, while USP5 reverses this process. A previous study showed that TRIM28 immunoprecipitated with METTL3, METTL14, and WTAP (Yue et al., 2018), which raised the possibility that TRIM28 could be a component of the m^6A writer complex. SPOP is known to mediate K48-linked ubiquitination and proteasome degradation of various substrates, such as estrogen receptors, PTEN, BRD4, MyD88, and PD-L1 (Wei et al., 2018). Interestingly, when SPOP oligomerizes with increased cellular level, it localizes to nuclear speckles (Marzahn et al., 2016), where METTL3-WTAP is located.

We observed K11, K48 and K63-linked polyubiquitination on METTL3 after USP5 knockdown. We also found that K11 ubiquitination of METTL3 can be elevated by USP5 inhibition and attenuated by ANAPC1 (subunit of anaphase-promoting complex, APC) knockdown. APC is the major E3 ligase that assembles K11-linked ubiquitin chain to drive proteasomal degradation and mitotic exit (Wickliffe et al., 2011). The abundance of K11 linkage strongly increases when APC is active during mitosis. In accordance with our observation, recently it was found that METTL3 is significantly downregulated during M phase (Fei et al., 2020). Elucidation of the post-translational and proteolysis degradation of METTL3 during cell cycle may shed further insights on how METTL3 contributes to normal cell differentiation and tumorigenesis.

METTL3/WTAP Phosphorylation by ERK is Important for mESCs Differentiation

Consistent with previous observations (Batista et al., 2014; Geula et al., 2015), our m^6A-seq data revealed extensive mRNA m^6A methylation in mESCs. Differentially methylated transcripts upon loss of METTL3/WTAP phosphorylation are enriched for genes involved in pluripotency and RNA processing, like those found in METTL3 KO studies. Our report suggests that ERK activation increases m^6A methylation on key pluripotent transcripts, thus contributing to their decay. Tuning the phosphorylation state of METTL3 could be an effective post-translational way to adjust global mRNA m^6A methylation.

While we found that phosphorylation of METTL3 affects its interaction with WTAP and USP5, interaction with other binding partners could also be affected. For instance, SMAD2/3 interacts with the METTL3-METT14-WTAP complex to promote m^6A binding to particular transcripts in mESCs (Bertero et al., 2018). ZFP217 has also been found to sequester METTL3, thereby restricting m^6A methylation of certain transcripts in ESCs (Aguilo et al., 2015). It would be interesting to determine whether METTL3 phosphorylation affects interaction with SMAD2/3 or ZFP217 in mESCs, which could further explain how phosphorylation of m^6A writer proteins can affect methylation of core pluripotency factor transcripts.

Other Pathways that May Regulate RNA m^6A Methylation

While our study sheds light on ERK phosphorylation of METTL3, other questions remain. First, what are other pathways that could regulate m^6A methylation? Pathways identified from Gene Ontology enrichment analysis for genes that promote m^6A include transcriptional regulation by TP53 and HIF-1 signaling. The same analysis for genes that apparently suppress m^6A include sphingosine-1-phosphate receptor signaling and protein targeting to

mitochondria (data not shown). Modulation of activity for these pathways may reveal more regulators of m^{6}A methylation.

Second, how does the interplay between different post-translational modifications of METTL3 affect its activity? METTL3 is not only phosphorylated but also SUMOylated (Du et al., 2018). SUMOylation of METTL3 reduces its methyltransferase activity, thereby lowering m^{6}A abundance. Intriguingly, MAPK activation can modulate SUMOylation; specifically, ERK activation de-SUMOylates the Elk-1 transcription factor (Yang et al., 2003; Yang and Sharrocks, 2010). It would be interesting to further explore whether METTL3 phosphorylation affects SUMOylation level.

Overall, our study sheds light on a signaling relationship between ERK pathway and m^{6}A methylation. Several challenges remain in understanding how cells regulate m^{6}A methylation spatiotemporally, as well as which transcripts are methylated. The post-translational regulation of m^{6}A writers, readers, and erasers may provide insight for these questions and could be an important factor in affecting the m^{6}A epitranscriptome.

Limitations

While our results support a model in which ERK phosphorylates m^{6}A methyltransferase components METTL3 and WTAP, leading to stabilization by USP5, our study is not without potential caveats. For instance, although we were able to identify ERK as an m^{6}A regulator, we noticed that not all known m^{6}A regulatory proteins were among the top-ranked gene in our genome-wide CRISPR screen. Part of the reason might be due to the use of a circular RNA reporter in our screen. How m^{6}A is installed on circRNA and how it affects translation could be different from mRNA. For example, YTHDF1 is not involved in the translation of circRNA (Di Timoteo et al., 2020). However, our targeted knockdown of METTL3, METTL14, WTAP, ALKBH5, and FTO did show expected reporter responses (Figure S1A).

We also showed that METTL3 can bind to USP5, and that this binding is promoted by ERK-mediated phosphorylation. This may be an example of how phosphorylation sites act as switches to regulate protein-protein interactions (Jin and Pawson, 2012). Based on expression of different USP5 protein domains, METTL3 appears to bind most strongly to the cryptic ZnF domain, which possesses multiple positively charged residues on the domain surface. Although there is no structure for WTAP and currently available structural data of METTL3 do not contain S43 and S50, prediction software (Sanchez-Garcia et al., 2019) suggests that METTL3 R523 is involved in the interaction with USP5. Its proximity to S525 likely suggests that S525 phosphorylation may increase binding affinity to a positively charged region of USP5. These findings would be strengthened with structural studies showing the binding site for USP5 on METTL3, as well as the phospho-sites of the METTL3-METTL14-WTAP structure.

STAR METHODS

RESOURCE AVAILABILITY

Lead Contact—Further information and requests for resources and reagents should be directed to the Lead Contact, Chuan He (chuanhe@uchicago.edu).

Materials Availability—Antibodies targeting the Ser43 phosphorylation of METTL3 were generated in collaboration with Lifetein LLC. There are restrictions to the availability of the anti-Ser43 phosphorylated METTL3 antibody due to the lack of an external centralized repository for its distribution and our need to maintain the stock. We are glad to share the antibody with reasonable compensation by requestor for its processing and shipping. All other unique/stable reagents generated in this study are available from the Lead Contact without restriction.

Data and Code Availability—The CRISPR screening and m^6A-seq data generated during this study are available at GSE138776. The human data for the skin cutaneous melanoma (SKCM) was derived from the The Cancer Genome Atlas (TCGA).

EXPERIMENTAL MODEL AND SUBJECT DETAILS

mESC culture and differentiation—mESCs were generated, maintained, and differentiated essentially as previously described (Geula et al., 2015). METTL3 knockout mESCs were kindly provided by Dr. Howard Y. Chang (Stanford University) and regularly tested negatively for mycoplasma contamination. Established ESC clones were genotyped by PCR and validated as METTL3-deficient by qPCR and Western blot. mESCs were cultured on mitomycin C-treated mouse embryonic fibroblasts in ES medium containing DMEM supplemented with 15% FBS, 1 mM L-glutamine, 0.1 mM mercaptoethanol, 1% non-essential amino acid, 1% penicillin/streptomycin, nucleosides 1,000 U /ml leukemia inhibitory factor, 3 μM CHIR99021 and 1 μM PD0325901. To observe the phenotype of METTL3-KO derived stable transfectants, 2μg/ml doxycycline were added to knock down WTAP through TetOn-shWTAP, 50 μg/ml cumate were added to induce CuO-METTL3-T2A-WTAP expression, and PD0325901 was removed from the medium to be able to compare the difference between WT and 3A2A. For embryoid body (EB) differentiation, 5×10^6 ESC were disaggregated with trypsin and transferred to non-adherent suspension culture dishes and cultured in MEF medium (DMEM supplemented with 1% L-Glutamine, 1% Non-essential amino acids, 1% penicillin/streptomycin and 15% FBS) for 8 days. The serum-free neural induction protocol was applied as described (Ying et al., 2003). ES cells were plated in 6-well plates at a density of $1.5X10^5$ cells/well in N2B27 medium with LIF (100 units/ml). The next day (day 0), the medium was changed to N2B27 without LIF. Medium was renewed daily thereafter.

Cell Culture—HeLa, 293T, 293TN, A375, CHL-1, MEL-624 cells were maintained in DMEM supplemented with 10% FBS and 1% penicillin/streptomycin. MCF-7, T47D, SKBR3, and HCT-116 cells were maintained in RPMI supplemented with 10% FBS and 1% penicillin/streptomycin. BT474 cells were maintained in RPMI supplemented with 20% FBS and 1% penicillin/streptomycin. To observe the phenotype of stable transfectants, 2 μg/ml

doxycycline was added to knock down WTAP and METTL3, while 50 μg/ml cumate was added to induce CuO-METTL3-T2A-WTAP expression.

METHOD DETAILS

Plasmids—The circRNA reporters containing split GFP with a m^6A motif were kindly provided by Z. Wang (Chinese Academy of Science, Shanghai, China) and subcloned into pCDH-CMV-MCS-EF1α-RFP (System Biosciences, CD512B-1). The CRISPR knockout pooled library (#1000000048), METTL3 (#53739), METTL14 (#53740), WTAP (#53741), pKMyc (#19400), Flag-ATM (#31985), ATR (#31611), Flag-IKKε (#26201), HA-GSK-3β (#14754), ERK1 (#23509), ERK2 (#23498), B-Raf V600E (#17544), HA-Ubiquitin (#17608), Ubiquitin-KO (#17603), Ubiquitin-K6 (#22900), Ubiquitin-K11 (#22901), Ubiquitin-K27 (#22902), Ubiquitin-K29 (#22903), Ubiquitin-K33 (#17603), Ubiquitin-48 (#17605), Ubiquitin-K63 (#17606), pMD2.G (#12259) and psPAX2 (#12260) were ordered from Addgene. Flag-IKKα, Flag-IKKβ, HA-AKT, Flag-mTOR, HA-MEKDD, HA-CDC2, FAK, EGFR, HER2 V659E, pCMV5-HA, and pCMV5-Flag were kindly provided by M.C. Hung (China Medical University, Taichung, Taiwan). pLightSwitch R01_3'UTR and *NANOG* 3'UTR were ordered from Switchgear Genomics. Mouse METTL3 (MR209093), mouse WTAP (MR216877), and human USP5 (RC224191) were purchased from OriGene. METTL3 (human and mice), METTL14, and WTAP were subcloned into pKMyc, METTL14 was subcloned into pCMV5-HA, and WTAP (human and mice), ERK1, ERK2, and USP5 were cloned into pCMV5-Flag. All mutants were generated using the QuikChange Site-Directed Mutagenesis Kit (Stratagene). The annealed shMETTL3 (TRCN0000289742), shWTAP (TRCN0000231424-human, TRCN0000124351-mice) specific targeted sequence was inserted into Tet-pLKO-puro (Addgene, #21915). Myc-METTL3-T2A-Flag-WTAP was cloned into pCDH-CuO-MCS-EF1α-RFP (System Biosciences, QM512B-1). pCDG-EF1α-CymR-T2A-Neo (QM400PA-2) for the cumate suppressor was ordered from System Biosciences. Human METTL3 was subcloned into the pLenti-DsRed_IRES_SNCA:EGFP lentiviral reporter (Addgene, #92195), after removing the SNCA gene from the plasmid in order to form a pLenti-DsRed-IRES-METTL3-EGFP reporter.

Transfection and Virus Production—For transient transfection, cells were transfected by Lipofectamine 2000 as previously described (Lee et al., 2007). Briefly, cells were seeded 24 hours before transfection, and the plasmid(s) and Lipofectamine reagent were combined in Opti-MEM media. Media was then replaced with regular media without antibiotics 6 hours later. For lentivirus production, a lentiviral construct (pCDH-CMV-MCS-EF1α-RFP plasmids for overexpressing circRNA-GFP, Tet-pLKO-puro for inducible knockdown of METTL3 or WTAP, pCDG-EF1α-CymR-T2A-Neo for cumate repressor, pCDH-CuO-MCS-EF1α-RFP for inducible overexpression of METTL3-T2A-WTAP, or pLenti-DsRed-IRES-METTL3-EGFP as METTL3 protein stability reporter) together with pMD2.G and psPAX2 were co-transfected into 293TN cells (System Biosciences). Viruses were concentrated by the PEG-it Virus Precipitation Solution and used for infecting cells in the presence of TransDux (System Biosciences). Pools of stable transfectants were selected by antibiotics or sorted by flow cytometry. Doxycycline (0.5 μg/mL) was used to induce shRNA while cumate (50 μg/mL) was used to induce shRNA-resistant cDNA expression.

Luciferase Reporter Assay—The luciferase plasmid LightSwitch 3'UTR Reporter, containing the *NANOG* 3'UTR or random negative control R01_3'UTR (Switchgear Genomics) was co-transfected with the m^6A writer complex and ERK-activated kinase into HeLa cells for two days. *NANOG* wild type RRACT 3'UTR reporter was mutated at 46A, 397A, and 743A (^{44}AAACT^{48}, ^{395}GGACT^{399}, ^{741}AAACT^{745}) to form a mutant RRTCT 3'UTR reporter. Luciferase expression was measured using the Luciferase Assay System according to the commercial protocol (Promega). *NANOG* 3'UTR luciferase activity was normalized to cells transfected with R01_3'UTR.

Flow Cytometry—Flow cytometry analysis was conducted on BD LSR Fortessa, and cell sorting was conducted on BD FACSAria Fusion. For SSEA-1 expression, cells were disaggregated with trypsin, blocked with TruStain FcX (BioLegend) then incubated with anti-SSEA-1 (BioLegend) in cell staining buffer (BioLegend).

CRISPR Screen—The genome-wide CRISPR-Cas9 gene knockdown screen was accomplished using GeCKOv2 gene knockout library following a published protocol (Joung et al., 2017). Briefly, the GeCKOV2 library was amplified in Endura electrocompetent cells (Lucigen) then co-transfected with pMD2.G and psPAX2 into 293TN cells to produce a lentiviral library. HeLa-circGFP cells were infected at 0.3 MOI for 3 days, then selected with 2 μg/ml puromycin for 1 week before flow cytometry sorting. Genomes of harvested cells were extracted by Quick-gDNA MidiPrep (Zymo). sgRNA after PCR amplification was sent to the University of Chicago Genomics Facility to be sequenced on Illumina HiSeq 4000 in single-end read mode. RIGER was used to analyze the sequencing results. To obtain the ranked difference plot, sgRNAs were ranked according to the difference between number of reads in low and high GFP populations. The top 1% of the sgRNAs that ranked with the greatest difference were selected for gene ontology enrichment analysis.

Immunoprecipitation, immunoblotting, *in vitro* kinase and deubiquitination assay—Immunoprecipitation (Jin et al.) and immunoblotting (IB) were performed as previously described (Sun et al., 2016). In brief, protein samples were isolated from respective cells by lysis in RIPA buffer (1% Triton X-100, 150 mM NaCl, 20 mM Na_2PO4, pH 7.4) containing Halt Protease and Phosphatase Inhibitor Cocktail (Thermo Scientific). Subsequently, a BCA assay (Thermo Scientific) was used to determine the protein concentrations. For IP, indicated antibody and protein A/G magnetic beads (Thermo Scientific) were incubated with lysate at 4°C overnight, followed by washing and elution with sample buffer (Bio-Rad). Equal amounts of protein were separated by SDS-PAGE followed by wet transfer to PVDF membranes. Blots were blocked with 5% non-fat milk or BSA and incubated with respective primary antibody at 4°C overnight. Primary antibodies were detected by HRP-linked secondary antibodies (Cell Signaling) together with SuperSignal West Pico Plus chemiluminescent substrate (Thermo Scientific) and imaged in a FluorChem R system (ProteinSimple). Densitometry calculations are calculated using ImageJ. To measure protein stability, cells were treated with 50 μg/mL cycloheximide (CHX) and harvested at 0, 6, and 12 hr.

Phosphate-affinity gel electrophoresis was performed in gels containing 60 μM $MnCl_2$, and 30 μM acrylamide-pendant Phos-tag ligand (AAL-107, Wako Chemicals). For *in vitro*

kinase assays, recombinant full-length kinase expressed in E. coli cells with an N-terminal GST tag, and N-terminal GST-tagged human METTL3/METTL14 complex expressed in Sf9 insect cells were purchased from SignalChem. Active kinase was diluted in Kinase Dilution Buffer III (SignalChem) and incubated with METTL3/METTL14 at 30°C for 15 min. The reaction was stopped by the addition of the sample buffer then analyzed by IB. For *in vitro* deubiquitination, 293T cells transfected with HA-ubiquitin were treated with 10 μM MG-132 and 10 μM EOAI3402143 for 8 hr. IP-purified METTL3 were incubated without or with purified USP5 (SignalChem) in deubiquitination buffer (SignalChem) following commercial protocol.

Confocal Microscopy—For confocal microscopy, cells after treatments were fixed in 4% paraformaldehyde, permeabilized with 0.5% Triton X-100, blocked with 5% bovine serum albumin, incubated with primary antibodies overnight at 4°C followed by incubation with the appropriate secondary antibody tagged with Alexa 488 or Alexa 568 (Molecular Probes). Nuclei were stained with 4’,6-diamidino-2-phenylindole (DAPI) before mounting. Confocal fluorescence images were captured using Olympus FV1000 confocal spectral microscope.

Mass Spectrometry—To identify phosphorylation sites of METTL3, METTL3 precipitated from 293T cells co-transfected with myc-METTL3 and B-Raf V600E was analyzed by Coomassie Blue staining. The protein band corresponding to METTL3 was excised and subjected to in-gel digestion with tryspin and chymotrypsin. Samples were analyzed by Ultimate Capillary LC system (Dionex) directly coupled to LTQ Orbitrap Mass Analyzer (Thermo Scientific) using the TopTenTM method. The data were searched on MASCOT (MassMatrix) against the human Swiss-Prot database. All the identified phospho-peptides were further confirmed by manually checking the results.

RNA Extraction and Real-Time qPCR—Total RNA was isolated using TRIzol (Invitrogen), and 200 ng of RNA was reversed transcribed into cDNA using PrimeScript RT Reagent Kit (Takara). Real-time qPCR was performed using the FastStart Essential DNA Green Master (Roche). HPRT1 was used as an internal control for normalization. Primers used in this study are listed in Table S5. For measuring RNA stability, cells were treated with 5 μg/ml actinomycin D and harvested at 0, 6, and 12 hr to determine the half-life of target mRNAs.

LC-MS/MS m^6A quantification of poly(A) RNA.—mRNA was extracted from the total RNA using 2 rounds of the Dynabeads mRNA Purification Kit (Thermo Scientific). 100 ng of mRNA was digested by nuclease P1 (1U) in 20 μl of buffer containing 20 mM NH_4OAc (pH = 5.3) at 42°C for 2 hr, followed by dephosphorylation with the addition of FastAP Thermosensitive Alkaline Phosphatase (1U) and FastAP buffer at 37°C for 2 hr. The sample was then diluted to 50 μl, and filtered (0.22 μm pore size, 4 mm diameter, Millipore). 5 μl of the solution was separated by reverse phase ultra-performance liquid chromatography on a C18 column, followed by online mass spectrometry detection using an Agilent 6410 QQQ triple-quadrupole LC mass spectrometer in positive electrospray ionization mode. The nucleosides were quantified by using the nucleoside-to-base ion mass transitions of 282 to 150 (m^6A) and 268 to 136 (A). Quantification was carried out by comparison with a

standard curve obtained from pure nucleoside. The ratio of m^6A to A was calculated based on the calibrated concentrations (Liu et al., 2018b).

m^6A-IP and m^6A-seq—m^6A-IP was performed using the EpiMark N6-Methyladenosine enrichment kit (NEB). Full length purified mRNA was used in m^6A-IP-qPCR. For m^6A-seq, mRNA was adjusted to 15 ng/μl in 100 μl and fragmented using a BioRuptor Ultrasonicator (Diagenode) with 30 s on/off for 30 cycles. Input and RNA eluted from m^6A-IP were used to prepare libraries with TruSeq Stranded mRNA Library Prep Kit (Illumina). Sequencing was carried out at the University of Chicago Genomics Facility on Illumina HiSeq 4000 in single-end read mode with 50 bp reads per read. Reads were aligned to the mycoplasma genome to assess contamination, followed by alignment to mouse genome version 10 (mm10) with HISAT2 v2.1.0 (Kim et al., 2015) with parameter –k 1.

The input library of m^6A sequencing was used for comparing gene expression levels. DESeq2 (Love et al., 2014) was applied for differential expression between R-WT and R-3A2A mESCs with FDR < 0.05 cutoff. m^6A-seq data were analyzed as described before (De Jesus et al., 2019). m^6A peak calling was performed using exomePeak R/Bioconductor package v 3.7 (Meng et al., 2013). Significant peaks with false discovery rate less than 0.05 were annotated to the RefSeq database (mm10). Homer v4.9.1 (Heinz et al., 2010) was used to search for the enriched motif in the m^6A peak region where random peaks of 200 bp were used as background sequences for motif discovery. m^6A peak distribution on the metagene was plotted by the R package Guitar (Cui et al., 2016).

Differential analysis of m^6A methylation was performed using the R package RADAR and MeRIPtools (Zhang et al., 2019b). To summarize and visualize the m^6A methylome data, principal component analysis (PCA) was performed using singular value decomposition approach implemented in R function (prcomp) on the log-transformed m^6A-IP data. Pathway and gene ontology enrichment analysis were performed using WebGestalt (Liao et al., 2019) with default settings. Pathway enrichment terms were determined using WikiPathway and KEGG terms.

Cell Proliferation Assay—Cells were seeded in 96-well plates. The cell proliferation was assessed by SRB assay (Vichai and Kirtikara, 2006) at various time points. Briefly, cells after treatments were fixed with 10% TCA then stained with 0.05% SRB. After washing 3–4 minutes with water, bound SRB was solubilized with 10 mM Trizma base and measured at 515nm.

Quantification of Histone Modifications—Histones were prepared from fresh cell pellets using Total Histone Extraction Kit (Epigentek). The efficiency of histone extraction was controlled by Coomassie Blue staining and IB with anti-H3 antibody. Histone posttranslational modifications were quantified using the Histone H3 Modification Multiplex Assay Kit (Epigentek) following commercial protocol. Each histogram corresponds to the mean of 2 independent experiments and each measure was obtained using a pool of 100 ng of total histones from 2 independent extractions.

Structural Analysis of Protein—The atomic coordinates and structure factors for the reported crystal structures were obtained from the Protein Data Bank (PDB) with the accession code 5IL0 for the ligand-free form of the METTL3-METTL14 complex and 3IHP for the covalent Ubiquitin-USP5 complex. All figures representing structures were prepared with PyMOL. The prediction of partner-specific protein interfaces was performed using the xgBoost based Interface Prediction of Specific Partner Interactions (BIPSPI) web server (Sanchez-Garcia et al., 2019). Predictions were performed using structural data using PDB atomic coordinates as described in the structural analysis of proteins.

QUANTIFICATION AND STATISTICAL ANALYSIS

Each experiment was performed at least three times, and representative data are shown. Data in the bar graphs are given as the mean ± SEM. Means were checked for statistical difference using Student's *t* test, and p-values < 0.05 were considered significant (*p < 0.05, **p < 0.01, ***p < 0.001). For survival analysis, Kaplan-Meier analysis and a log rank test were applied.

Supplementary Material

Refer to Web version on PubMed Central for supplementary material.

Acknowledgements

We thank the Genomics Facility, Integrated Light Microscopy Core Facility, and Flow Cytometry Core Facility at the University of Chicago for technical support. We also thank the Mass Spectrometry Facility at Ohio State University. This work was supported by NIH grants F32 CA221007 (B.T.H.), CA247175 (A.C.Z.), and HG008935 (C.H.). C.H. is an investigator of the Howard Hughes Medical Institute.

References:

Aguilo F, Zhang F, Sancho A, Fidalgo M, Di Cecilia S, Vashisht A, Lee DF, Chen CH, Rengasamy M, Andino B, et al. (2015). Coordination of m(6)A mRNA Methylation and Gene Transcription by ZFP217 Regulates Pluripotency and Reprogramming. Cell Stem Cell 17, 689–704. [PubMed: 26526723]

Avvakumov GV, Walker JR, Xue S, Allali-Hassani A, Asinas A, Nair UB, Fang X, Zuo X, Wang YX, Wilkinson KD, et al. (2012). Two ZnF-UBP domains in isopeptidase T (USP5). Biochemistry 51, 1188–1198. [PubMed: 22283393]

Batista PJ, Molinie B, Wang J, Qu K, Zhang J, Li L, Bouley DM, Lujan E, Haddad B, Daneshvar K, et al. (2014). m(6)A RNA modification controls cell fate transition in mammalian embryonic stem cells. Cell Stem Cell 15, 707–719. [PubMed: 25456834]

Bennetzen MV, Larsen DH, Bunkenborg J, Bartek J, Lukas J, and Andersen JS (2010). Site-specific phosphorylation dynamics of the nuclear proteome during the DNA damage response. Mol Cell Proteomics 9, 1314–1323. [PubMed: 20164059]

Bertero A, Brown S, Madrigal P, Osnato A, Ortmann D, Yiangou L, Kadiwala J, Hubner NC, de Los Mozos IR, Sadee C, et al. (2018). The SMAD2/3 interactome reveals that TGFbeta controls m(6)A mRNA methylation in pluripotency. Nature 555, 256–259. [PubMed: 29489750]

Casar B, Pinto A, and Crespo P (2009). ERK dimers and scaffold proteins: unexpected partners for a forgotten (cytoplasmic) task. Cell Cycle 8, 1007–1013. [PubMed: 19279408]

Choe J, Lin S, Zhang W, Liu Q, Wang L, Ramirez-Moya J, Du P, Kim W, Tang S, Sliz P, et al. (2018). mRNA circularization by METTL3-eIF3h enhances translation and promotes oncogenesis. Nature 561, 556–560. [PubMed: 30232453]

Cui X., Wei Z., Zhang L., Liu H., Sun L., Zhang SW., Huang Y., and Meng J. (2016). Guitar: An R/Bioconductor Package for Gene Annotation Guided Transcriptomic Analysis of RNA-Related Genomic Features. Biomed Res Int 2016, 8367534. [PubMed: 27239475]

De Jesus DF, Zhang Z, Kahraman S, Brown NK, Chen M, Hu J, Gupta MK, He C, and Kulkarni RN (2019). m6A mRNA methylation regulates human β-cell biology in physiological states and in type 2 diabetes. Nature Metabolism 1, 765–774.

Deng R, Cheng Y, Ye S, Zhang J, Huang R, Li P, Liu H, Deng Q, Wu X, Lan P, et al. (2019). m(6)A methyltransferase METTL3 suppresses colorectal cancer proliferation and migration through p38/ERK pathways. Onco Targets Ther 12, 4391–4402. [PubMed: 31239708]

Desideri E, Cavallo AL, and Baccarini M (2015). Alike but Different: RAF Paralogs and Their Signaling Outputs. Cell 161, 967–970. [PubMed: 26000477]

Di Timoteo G, Dattilo D, Centron-Broco A, Colantoni A, Guarnacci M, Rossi F, Incarnato D, Oliviero S, Fatica A, Morlando M, et al. (2020). Modulation of circRNA Metabolism by m(6)A Modification. Cell Rep 31, 107641. [PubMed: 32402287]

Dominissini D, Moshitch-Moshkovitz S, Schwartz S, Salmon-Divon M, Ungar L, Osenberg S, Cesarkas K, Jacob-Hirsch J, Amariglio N, Kupiec M, et al. (2012). Topology of the human and mouse m6A RNA methylomes revealed by m6A-seq. Nature 485, 201–206. [PubMed: 22575960]

Du Y, Hou G, Zhang H, Dou J, He J, Guo Y, Li L, Chen R, Wang Y, Deng R, et al. (2018). SUMOylation of the m6A-RNA methyltransferase METTL3 modulates its function. Nucleic Acids Res 46, 5195–5208. [PubMed: 29506078]

Fei Q, Zou Z, Roundtree IA, Sun HL, and He C (2020). YTHDF2 promotes mitotic entry and is regulated by cell cycle mediators. PLoS Biol 18, e3000664. [PubMed: 32267835]

Feng Z, Li Q, Meng R, Yi B, and Xu Q (2018). METTL3 regulates alternative splicing of MyD88 upon the lipopolysaccharide-induced inflammatory response in human dental pulp cells. J Cell Mol Med 22, 2558–2568. [PubMed: 29502358]

Frye M, Harada BT, Behm M, and He C (2018). RNA modifications modulate gene expression during development. Science 361, 1346–1349. [PubMed: 30262497]

Geula S, Moshitch-Moshkovitz S, Dominissini D, Mansour AA, Kol N, Salmon-Divon M, Hershkovitz V, Peer E, Mor N, Manor YS, et al. (2015). Stem cells. m6A mRNA methylation facilitates resolution of naive pluripotency toward differentiation. Science 347, 1002–1006. [PubMed: 25569111]

Guillamot M, Ouazia D, Dolgalev I, Yeung ST, Kourtis N, Dai Y, Corrigan K, Zea-Redondo L, Saraf A, Florens L, et al. (2019). The E3 ubiquitin ligase SPOP controls resolution of systemic inflammation by triggering MYD88 degradation. Nat Immunol 20, 1196–1207. [PubMed: 31406379]

Heinz S, Benner C, Spann N, Bertolino E, Lin YC, Laslo P, Cheng JX, Murre C, Singh H, and Glass CK (2010). Simple combinations of lineage-determining transcription factors prime cis-regulatory elements required for macrophage and B cell identities. Mol Cell 38, 576–589. [PubMed: 20513432]

Jia G, Fu Y, Zhao X, Dai Q, Zheng G, Yang Y, Yi C, Lindahl T, Pan T, Yang YG, et al. (2011). N6-methyladenosine in nuclear RNA is a major substrate of the obesity-associated FTO. Nat Chem Biol 7, 885–887. [PubMed: 22002720]

Jin J, and Pawson T (2012). Modular evolution of phosphorylation-based signalling systems. Philos Trans R Soc Lond B Biol Sci 367, 2540–2555. [PubMed: 22889906]

Jin L, Williamson A, Banerjee S, Philipp I, and Rape M (2008). Mechanism of ubiquitin-chain formation by the human anaphase-promoting complex. Cell 133, 653–665. [PubMed: 18485873]

Joung J, Konermann S, Gootenberg JS, Abudayyeh OO, Platt RJ, Brigham MD, Sanjana NE, and Zhang F (2017). Genome-scale CRISPR-Cas9 knockout and transcriptional activation screening. Nat Protoc 12, 828–863. [PubMed: 28333914]

Kim D, Langmead B, and Salzberg SL (2015). HISAT: a fast spliced aligner with low memory requirements. Nat Methods 12, 357–360. [PubMed: 25751142]

Kinoshita E, Kinoshita-Kikuta E, Takiyama K, and Koike T (2006). Phosphate-binding tag, a new tool to visualize phosphorylated proteins. Mol Cell Proteomics 5, 749–757. [PubMed: 16340016]

Kobayashi M, Ohsugi M, Sasako T, Awazawa M, Umehara T, Iwane A, Kobayashi N, Okazaki Y, Kubota N, Suzuki R, et al. (2018). The RNA Methyltransferase Complex of WTAP, METTL3, and METTL14 Regulates Mitotic Clonal Expansion in Adipogenesis. Mol Cell Biol 38.

Kunath T, Saba-El-Leil MK, Almousailleakh M, Wray J, Meloche S, and Smith A (2007). FGF stimulation of the Erk1/2 signalling cascade triggers transition of pluripotent embryonic stem cells from self-renewal to lineage commitment. Development 134, 2895–2902. [PubMed: 17660198]

Lee DF, Kuo HP, Chen CT, Hsu JM, Chou CK, Wei Y, Sun HL, Li LY, Ping B, Huang WC, et al. (2007). IKK beta suppression of TSC1 links inflammation and tumor angiogenesis via the mTOR pathway. Cell 130, 440–455. [PubMed: 17693255]

Leicht DT, Balan V, Kaplun A, Singh-Gupta V, Kaplun L, Dobson M, and Tzivion G (2007). Raf kinases: function, regulation and role in human cancer. Biochim Biophys Acta 1773, 1196–1212. [PubMed: 17555829]

Lever J, Zhao EY, Grewal J, Jones MR, and Jones SJM (2019). CancerMine: a literature-mined resource for drivers, oncogenes and tumor suppressors in cancer. Nat Methods 16, 505–507. [PubMed: 31110280]

Liao Y, Wang J, Jaehnig EJ, Shi Z, and Zhang B (2019). WebGestalt 2019: gene set analysis toolkit with revamped UIs and APIs. Nucleic Acids Res 47, W199–W205. [PubMed: 31114916]

Lin S, Choe J, Du P, Triboulet R, and Gregory RI (2016). The m(6)A Methyltransferase METTL3 Promotes Translation in Human Cancer Cells. Mol Cell 62, 335–345. [PubMed: 27117702]

Lito P, Saborowski A, Yue J, Solomon M, Joseph E, Gadal S, Saborowski M, Kastenhuber E, Fellmann C, Ohara K, et al. (2014). Disruption of CRAF-mediated MEK activation is required for effective MEK inhibition in KRAS mutant tumors. Cancer Cell 25, 697–710. [PubMed: 24746704]

Liu F, Yang X, Geng M, and Huang M (2018a). Targeting ERK, an Achilles' Heel of the MAPK pathway, in cancer therapy. Acta Pharm Sin B 8, 552–562. [PubMed: 30109180]

Liu J, Eckert MA, Harada BT, Liu SM, Lu Z, Yu K, Tienda SM, Chryplewicz A, Zhu AC, Yang Y, et al. (2018b). m(6)A mRNA methylation regulates AKT activity to promote the proliferation and tumorigenicity of endometrial cancer. Nat Cell Biol 20, 1074–1083. [PubMed: 30154548]

Liu J, Yue Y, Han D, Wang X, Fu Y, Zhang L, Jia G, Yu M, Lu Z, Deng X, et al. (2014). A METTL3-METTL14 complex mediates mammalian nuclear RNA N6-adenosine methylation. Nat Chem Biol 10, 93–95. [PubMed: 24316715]

Love MI, Huber W, and Anders S (2014). Moderated estimation of fold change and dispersion for RNA-seq data with DESeq2. Genome Biol 15, 550. [PubMed: 25516281]

Marzahn MR, Marada S, Lee J, Nourse A, Kenrick S, Zhao H, Ben-Nissan G, Kolaitis RM, Peters JL, Pounds S, et al. (2016). Higher-order oligomerization promotes localization of SPOP to liquid nuclear speckles. EMBO J 35, 1254–1275. [PubMed: 27220849]

Matsuoka S, Ballif BA, Smogorzewska A, McDonald ER 3rd, Hurov KE, Luo J, Bakalarski CE, Zhao Z, Solimini N, Lerenthal Y, et al. (2007). ATM and ATR substrate analysis reveals extensive protein networks responsive to DNA damage. Science 316, 1160–1166. [PubMed: 17525332]

Meng J, Cui X, Rao MK, Chen Y, and Huang Y (2013). Exome-based analysis for RNA epigenome sequencing data. Bioinformatics 29, 1565–1567. [PubMed: 23589649]

Meyer KD, Saletore Y, Zumbo P, Elemento O, Mason CE, and Jaffrey SR (2012). Comprehensive analysis of mRNA methylation reveals enrichment in 3' UTRs and near stop codons. Cell 149, 1635–1646. [PubMed: 22608085]

Ping XL, Sun BF, Wang L, Xiao W, Yang X, Wang WJ, Adhikari S, Shi Y, Lv Y, Chen YS, et al. (2014). Mammalian WTAP is a regulatory subunit of the RNA N6-methyladenosine methyltransferase. Cell Res 24, 177–189. [PubMed: 24407421]

Potu H, Peterson LF, Pal A, Verhaegen M, Cao J, Talpaz M, and Donato NJ (2014). Usp5 links suppression of p53 and FAS levels in melanoma to the BRAF pathway. Oncotarget 5, 5559–5569. [PubMed: 24980819]

Raasi S, Varadan R, Fushman D, and Pickart CM (2005). Diverse polyubiquitin interaction properties of ubiquitin-associated domains. Nat Struct Mol Biol 12, 708–714. [PubMed: 16007098]

Roskoski R Jr. (2012). ERK1/2 MAP kinases: structure, function, and regulation. Pharmacol Res 66, 105–143. [PubMed: 22569528]

Sanchez-Garcia R, Sorzano COS, Carazo JM, and Segura J (2019). BIPSPI: a method for the prediction of partner-specific protein-protein interfaces. Bioinformatics 35, 470–477. [PubMed: 30020406]

Schadendorf D, van Akkooi ACJ, Berking C, Griewank KG, Gutzmer R, Hauschild A, Stang A, Roesch A, and Ugurel S (2018). Melanoma. Lancet 392, 971–984. [PubMed: 30238891]

Shi H, Wang X, Lu Z, Zhao BS, Ma H, Hsu PJ, Liu C, and He C (2017). YTHDF3 facilitates translation and decay of N(6)-methyladenosine-modified RNA. Cell Res 27, 315–328. [PubMed: 28106072]

Sun HL, Cui R, Zhou J, Teng KY, Hsiao YH, Nakanishi K, Fassan M, Luo Z, Shi G, Tili E, et al. (2016). ERK Activation Globally Downregulates miRNAs through Phosphorylating Exportin-5. Cancer Cell 30, 723–736. [PubMed: 27846390]

Vichai V, and Kirtikara K (2006). Sulforhodamine B colorimetric assay for cytotoxicity screening. Nat Protoc 1, 1112–1116. [PubMed: 17406391]

Wang H., Hu X., Huang M., Liu J., Gu Y., Ma L., Zhou Q., and Cao X. (2019). Mettl3-mediated mRNA m(6)A methylation promotes dendritic cell activation. Nat Commun 10, 1898. [PubMed: 31015515]

Wang P, Doxtader KA, and Nam Y (2016). Structural Basis for Cooperative Function of Mettl3 and Mettl14 Methyltransferases. Mol Cell 63, 306–317. [PubMed: 27373337]

Wang X, Lu Z, Gomez A, Hon GC, Yue Y, Han D, Fu Y, Parisien M, Dai Q, Jia G, et al. (2014a). N6-methyladenosine-dependent regulation of messenger RNA stability. Nature 505, 117–120. [PubMed: 24284625]

Wang X, Zhao BS, Roundtree IA, Lu Z, Han D, Ma H, Weng X, Chen K, Shi H, and He C (2015). N(6)-methyladenosine Modulates Messenger RNA Translation Efficiency. Cell 161, 1388–1399. [PubMed: 26046440]

Wang Y, Li Y, Toth JI, Petroski MD, Zhang Z, and Zhao JC (2014b). N6-methyladenosine modification destabilizes developmental regulators in embryonic stem cells. Nat Cell Biol 16, 191–198. [PubMed: 24394384]

Wang Y, Li Y, Yue M, Wang J, Kumar S, Wechsler-Reya RJ, Zhang Z, Ogawa Y, Kellis M, Duester G, et al. (2018). N(6)-methyladenosine RNA modification regulates embryonic neural stem cell self-renewal through histone modifications. Nat Neurosci 21, 195–206. [PubMed: 29335608]

Wei X, Fried J, Li Y, Hu L, Gao M, Zhang S, and Xu B (2018). Functional roles of Speckle-Type Poz (SPOP) Protein in Genomic stability. J Cancer 9, 3257–3262. [PubMed: 30271484]

Wickliffe KE, Williamson A, Meyer HJ, Kelly A, and Rape M (2011). K11-linked ubiquitin chains as novel regulators of cell division. Trends Cell Biol 21, 656–663. [PubMed: 21978762]

Xiang Y, Laurent B, Hsu CH, Nachtergaele S, Lu Z, Sheng W, Xu C, Chen H, Ouyang J, Wang S, et al. (2017). RNA m(6)A methylation regulates the ultraviolet-induced DNA damage response. Nature 543, 573–576. [PubMed: 28297716]

Xiao W, Adhikari S, Dahal U, Chen YS, Hao YJ, Sun BF, Sun HY, Li A, Ping XL, Lai WY, et al. (2016). Nuclear m(6)A Reader YTHDC1 Regulates mRNA Splicing. Mol Cell 61, 507–519. [PubMed: 26876937]

Yang SH, Jaffray E, Hay RT, and Sharrocks AD (2003). Dynamic interplay of the SUMO and ERK pathways in regulating Elk-1 transcriptional activity. Mol Cell 12, 63–74. [PubMed: 12887893]

Yang SH, and Sharrocks AD (2010). MAP Kinase: SUMO pathway interactions. Methods Mol Biol 661, 343–367. [PubMed: 20811994]

Yang Y, Fan X, Mao M, Song X, Wu P, Zhang Y, Jin Y, Yang Y, Chen LL, Wang Y, et al. (2017). Extensive translation of circular RNAs driven by N(6)-methyladenosine. Cell Res 27, 626–641. [PubMed: 28281539]

Yen HC, Xu Q, Chou DM, Zhao Z, and Elledge SJ (2008). Global protein stability profiling in mammalian cells. Science 322, 918–923. [PubMed: 18988847]

Ying QL, Stavridis M, Griffiths D, Li M, and Smith A (2003). Conversion of embryonic stem cells into neuroectodermal precursors in adherent monoculture. Nat Biotechnol 21, 183–186. [PubMed: 12524553]

Zhang C, Samanta D, Lu H, Bullen JW, Zhang H, Chen I, He X, and Semenza GL (2016). Hypoxia induces the breast cancer stem cell phenotype by HIF-dependent and ALKBH5-mediated m(6)A-

demethylation of NANOG mRNA. Proc Natl Acad Sci U S A 113, E2047–2056. [PubMed: 27001847]

Zhang Y, Gu X, Li D, Cai L, and Xu Q (2019a). METTL3 Regulates Osteoblast Differentiation and Inflammatory Response via Smad Signaling and MAPK Signaling. Int J Mol Sci 21.

Zhang Z, Zhan Q, Eckert M, Zhu A, Chryplewicz A, De Jesus DF, Ren D, Kulkarni RN, Lengyel E, He C, et al. (2019b). RADAR: differential analysis of MeRIP-seq data with a random effect model. Genome Biol 20, 294. [PubMed: 31870409]

Zheng G, Dahl JA, Niu Y, Fedorcsak P, Huang CM, Li CJ, Vagbo CB, Shi Y, Wang WL, Song SH, et al. (2013). ALKBH5 is a mammalian RNA demethylase that impacts RNA metabolism and mouse fertility. Mol Cell 49, 18–29. [PubMed: 23177736]

Zhou KI., Shi H., Lyu R., Wylder AC., Matuszek Z., Pan JN., He C., Parisien M., and Pan T. (2019). Regulation of Co-transcriptional Pre-mRNA Splicing by m(6)A through the Low-Complexity Protein hnRNPG. Mol Cell 76, 70–81 e79. [PubMed: 31445886]

Zong X, Zhao J, Wang H, Lu Z, Wang F, Du H, and Wang Y (2019). Mettl3 Deficiency Sustains Long-Chain Fatty Acid Absorption through Suppressing Traf6-Dependent Inflammation Response. J Immunol 202, 567–578. [PubMed: 30567729]

Highlights

1. Activation of the ERK pathway phosphorylates METTL3 and WTAP.
2. METTL3 phosphorylation increases USP5-mediated deubiquitination to stabilize METTL3.
3. Phosphorylation of METTL3 promotes mESC differentiation.
4. METTL3 phosphorylation in ERK-activated tumor cells contributes to tumorigenesis.

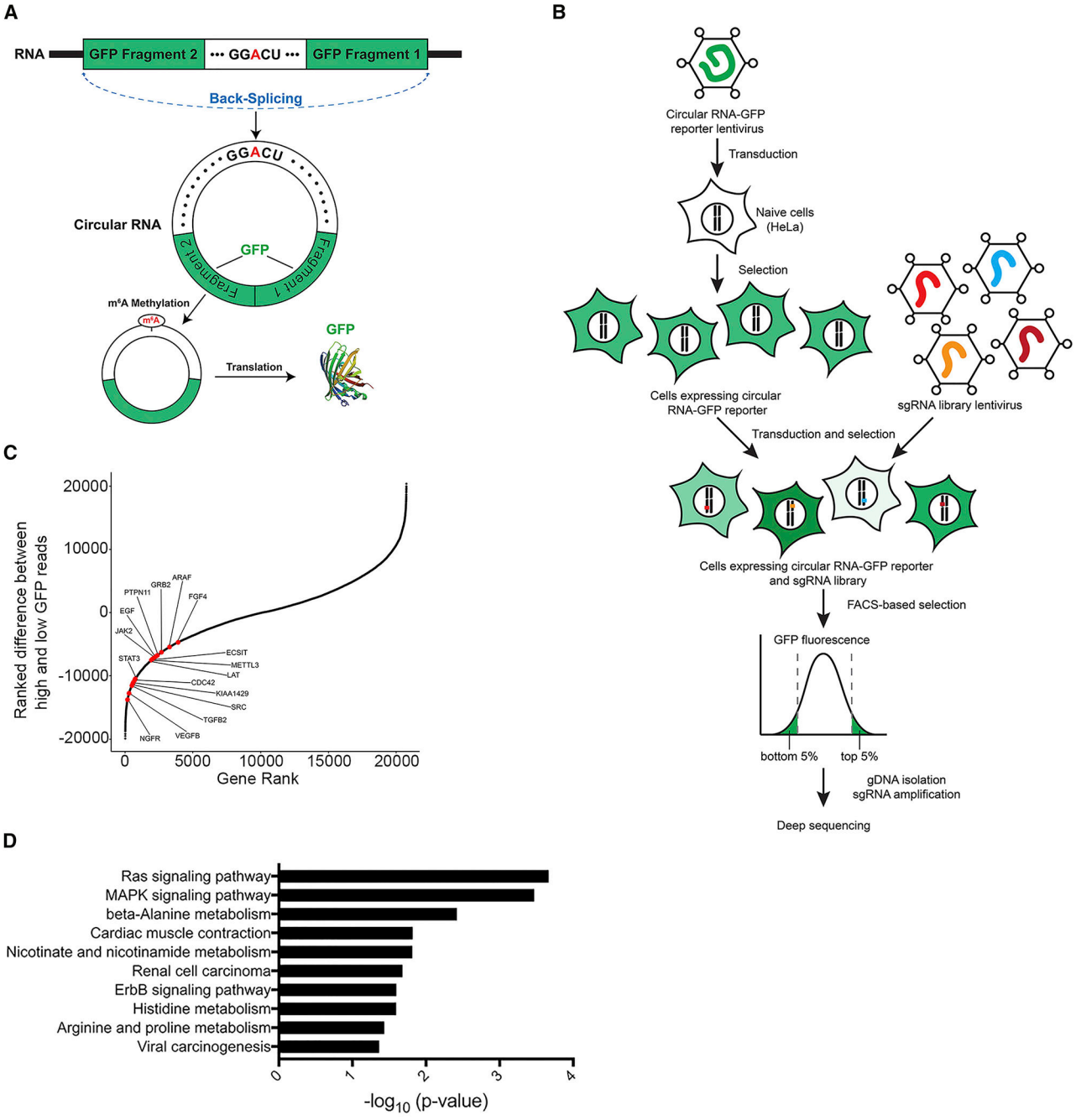

Figure 1. ERK Activation Promotes mRNA m^{6}A Methylation

(A) Schematic diagram of a circular RNA (circRNA) translation reporter consisting of a single exon and two introns with complementary sequences. The exon containing GGACU can be back-spliced to generate circRNAs that drive GFP translation.

(B) Overview of the CRISPR screen. Cas9 KO libraries are packaged into lentivirus and then transduced into HeLa cells contain circRNA GFP reporters. Cells with the top and bottom 5% GFP expression were collected by flow cytometry. The sgRNA were amplified from genomic DNA and then sequenced, followed by statistical analyses to identify candidate genes.

(C) Positive regulators for the m^6A pathway identified in the screen using circular GGACU-GFP reporters.

(D) Pathway analysis of sgRNA enriched in the bottom 5% GFP cells with circRNA GFP reporters.

See also Figure S1, Table S1, and Table S2.

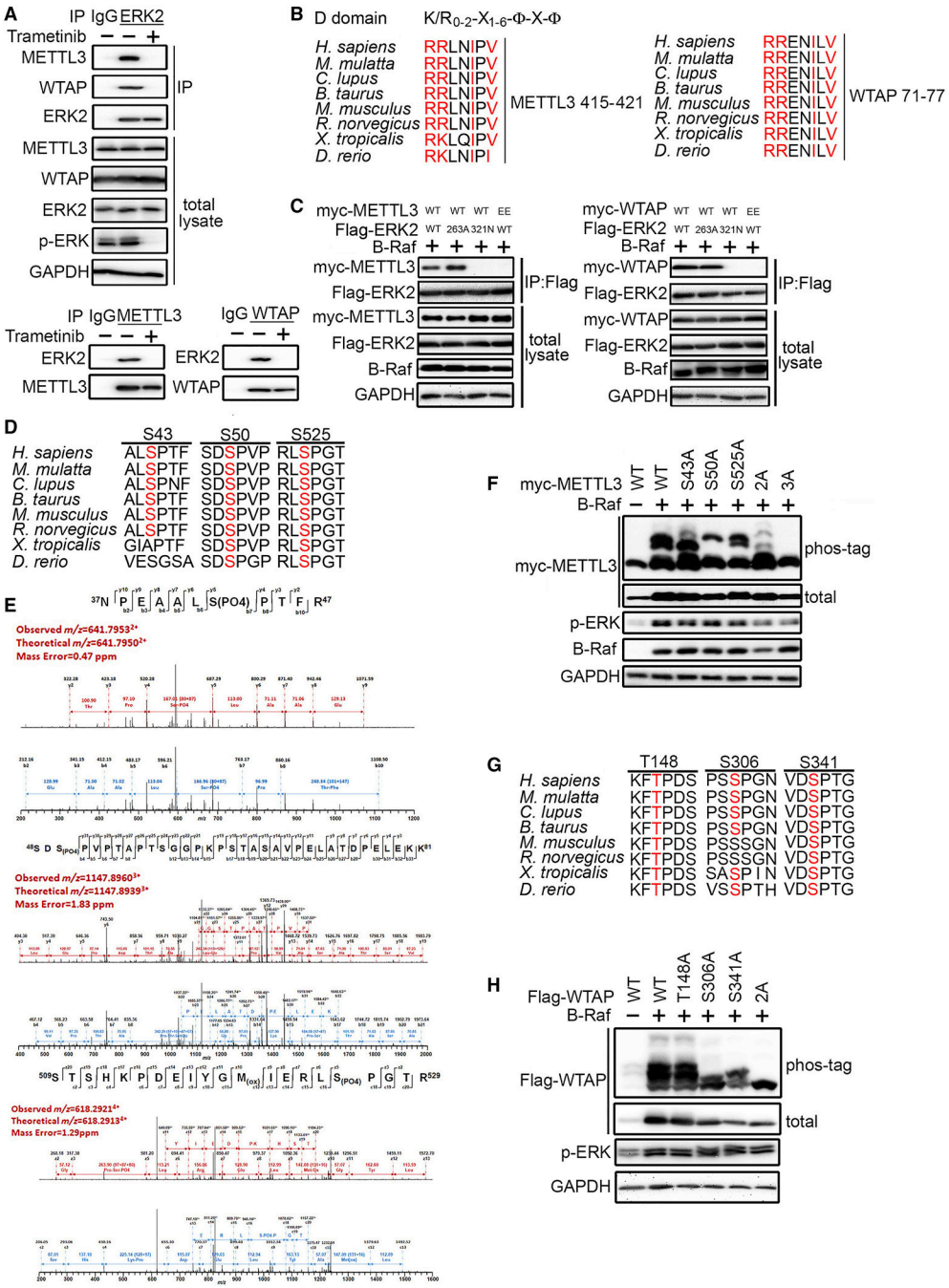

Figure 2. ERK Interacts and Phosphorylates METTL3 and WTAP

(A) A375 cells were treated with/without 0.1 μM trametinib for 1 hr. Lysates were analyzed by IP and IB as indicated.

(B) Sequence alignment of the conserved D-domain on METTL3 and WTAP predicted by the ELM website. The D domain possesses a consensus binding sequence of (Lys/Arg)0–2-(X)1–6-Φ-X-Φ; where Φ is a hydrophobic residue such as Leu, Ile, Val, Phe, and X is any amino acid.

(C) Interaction between wild-type (WT) or mutant METTL3, WTAP, and ERK2 in lysates from BRAF-expressing 293T cells transfected as indicated was examined by co-IP. EE, R415E/R416E METTL3 or R71E/R72E WTAP.

(D) Sequence alignment of the conserved serine residues on METTL3 that are phosphorylated by ERK.

(E) Mass spectrometry detected S43, S50 and S525 phosphorylation in METTL3 in 293T cells co-transfected with BRAF V600E.

(F) Phos-tag SDS-PAGE showing the phosphorylation status of WT or non-phosphorylatable alanine mutants of METTL3 in 293T cells co-transfected with BRAF. 2A, T43A/S50A; 3A, S43A/S50A/S525A.

(G) Sequence alignment of the serine/threonine-proline (S/T-P) motif on WTAP.

(H) Phos-tag SDS-PAGE showing the phosphorylation status of WT or non-phosphorylatable alanine mutants of human WTAP in 293T cells co-transfected with BRAF. 2A, S306A/S341A.

See also Figure S2.

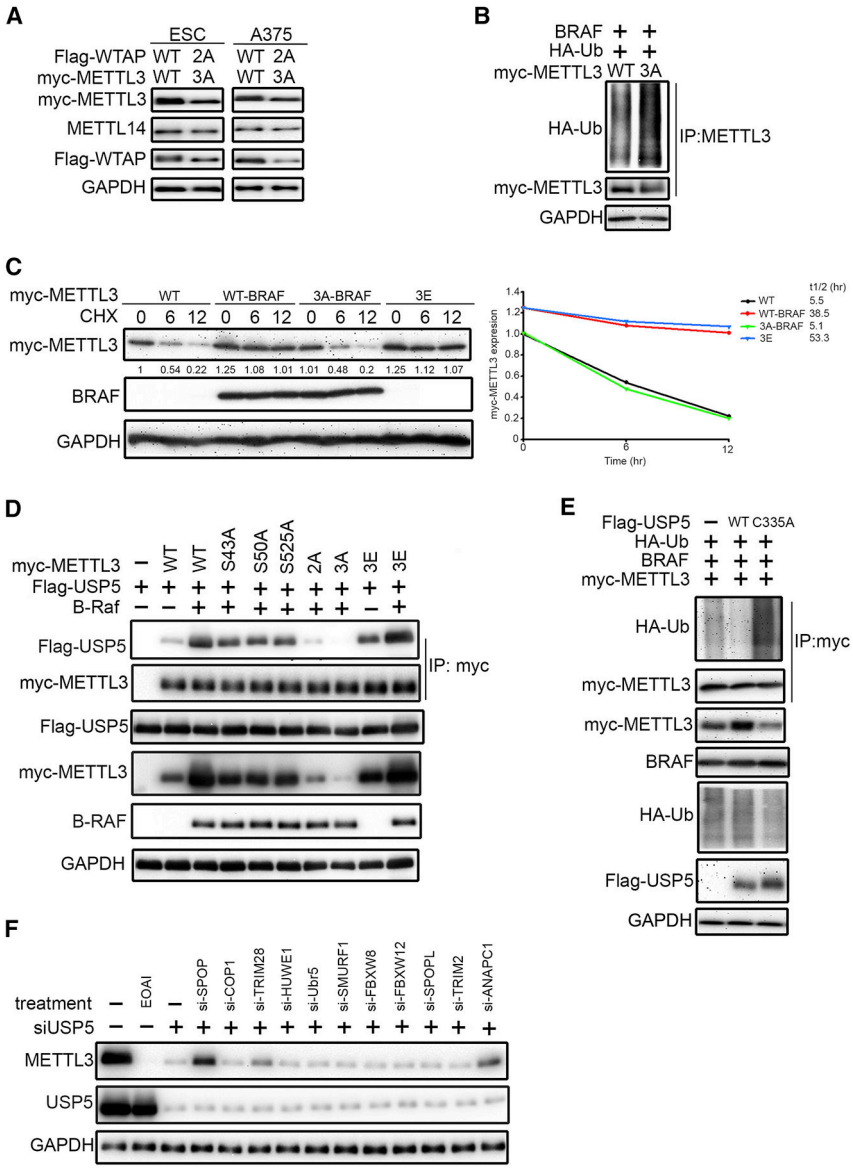

Figure 3. USP5 is Required for ERK-Mediated METTL3 Stabilization

(A) Comparison of METTL3 and WTAP protein levels in mESCs and A375 stable transfectants by immunoblotting (IB).

(B) 293T cells transfected as indicated were treated with MG-132 (10 μM, 8hr) followed by IP/IB.

(C) 293T cells transfected as indicated for 48 hr, followed by cycloheximide (CHX) 10 μg/ml for 0–12 h. Lysates were used for IB to measure the protein levels of METTL3. Density of METTL3 expression was quantified by ImageJ and the relative fold compared to the untreated WT was indicated and plotted at the right panel.

(D) BRAF expression promotes METTL3-USP5 interaction. Lysates of 293T cells transfected as indicated for 48 hr were subjected to IP with anti-myc antibody followed by IB.

(E) USP5 decreases ubiquitination of METTL3. Lysates of 293T cells transfected as indicated for 48 hr were subjected to IP with anti-myc antibody followed by IB.
(F) Knockdown of SPOP, TRIM28, and ANAPC1 attenuated USP5 inhibition-induced degradation of METTL3. A375 cells were transfected with siRNA for 72 hr or treated with 10 μM EOAI3402143 (EOAI) for 8 hr before IB analysis.
See also Figure S3 and Figure S4.

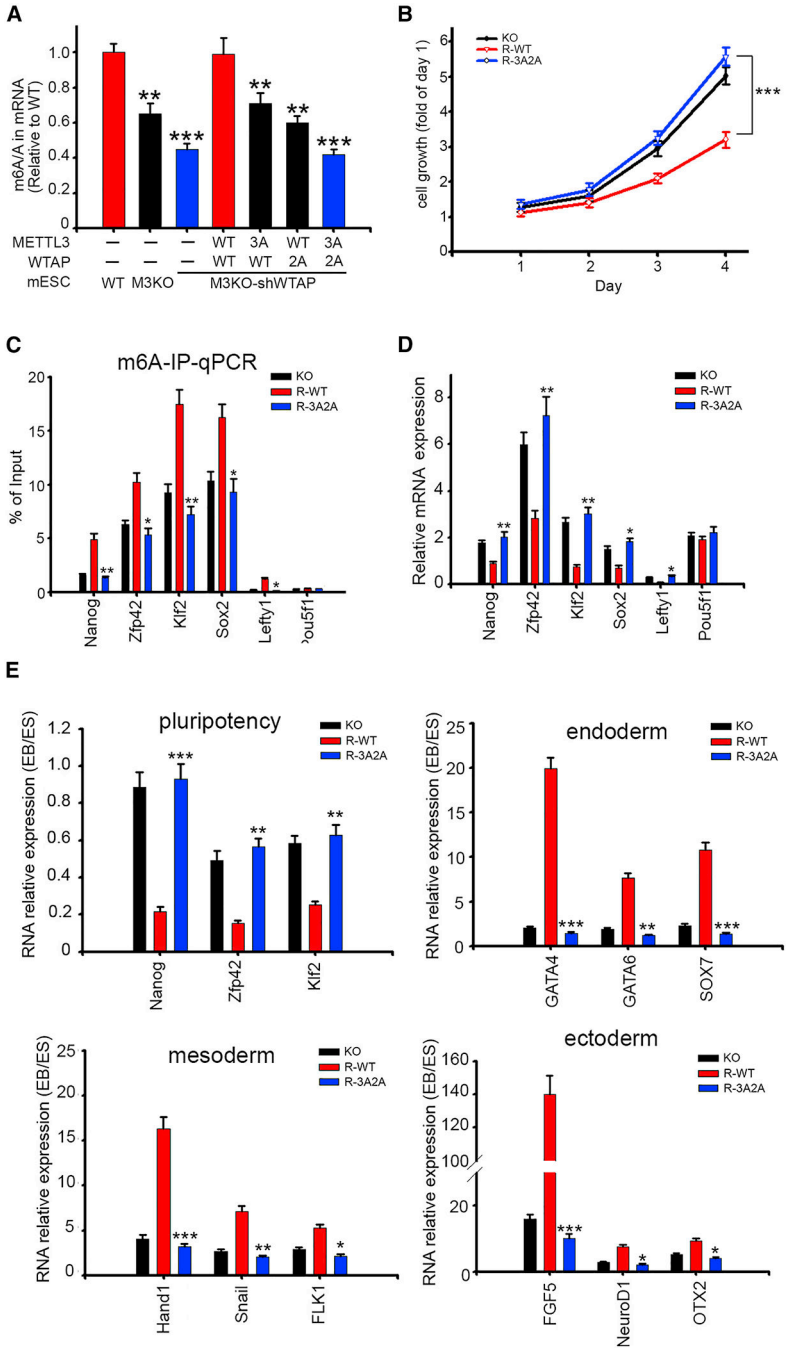

Figure 4. Phosphorylation of METTL3/WTAP by ERK Facilitates Resolution of Pluripotency

(A) LC-MS/MS quantification of the m^6A/A ratio in mRNA of mESCs stable transfectants. *p < 0.05, **p < 0.01, ***p < 0.001.

(B) Cell growth of R-WT and R-3A2A mESCs were measured by sulforhodamine B dye (SRB assay). Data are presented as relative to Day 1. ***p < 0.001.

(C) MeRIP-qPCR of pluripotency transcripts in mESCs stable transfectants. *p < 0.05, **p < 0.01.

(D) qPCR analysis of pluripotency genes in mESCs stable transfectants. *p < 0.05, **p < 0.01. (E) qPCR analysis for pluripotency and differentiation markers expression after 8 days of embryonic body induction. *p < 0.05, **p < 0.01, ***p < 0.001.
Unless otherwise indicated, all data in this figure contain n = 3 replicates per group, and represent mean ± SEM. All p-values were also calculated by Student's *t* test.
See also Figure S5.

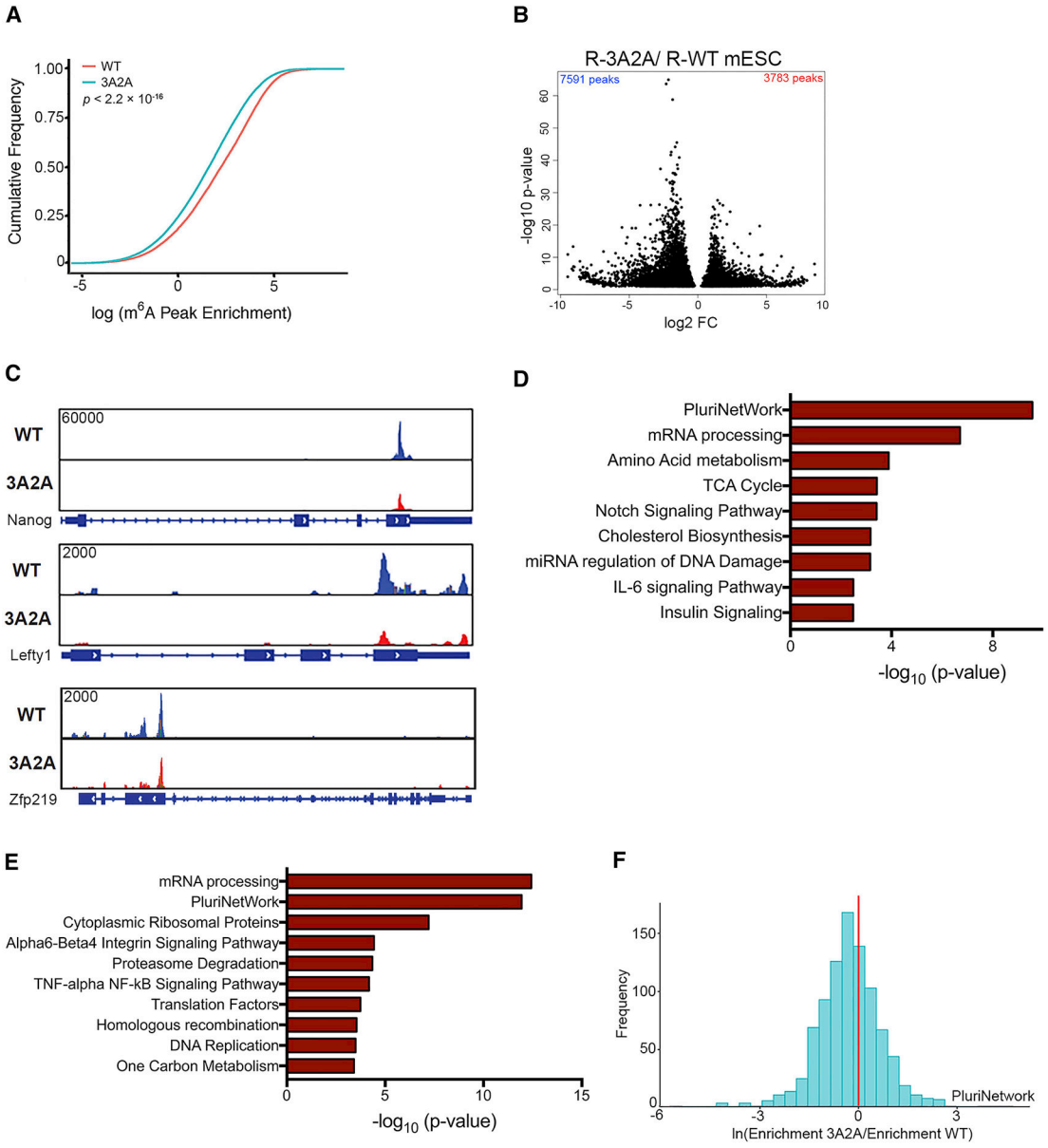

Figure 5. Transcripts Affected by Phosphorylation of Methyltransferase Complex in mESCs

(A) Cumulative distribution function of log2 peak intensity of m^{6}A-modified sites in R-WT and R-3A2A mESCs.

(B) Volcano plot for peaks with differential m^{6}A intensity between R-WT and R-3A2A mESCs. Fold change (FC) is the ratio of IP over Input for R-WT and R-3A2A.

(C) Coverage plots of the m^{6}A peaks of *Nanog*, *Lefty1*, and *Zfp219* comparing R-WT and R-3A2A mESCs. Plotted coverages are the medians of three replicates.

(D) Gene enrichment analysis with WikiPathway terms of differentially m^{6}A methylated peaks in R-WT and R-3A2A mESCs for molecular functions.

(E) Gene enrichment analysis with WikiPathway terms of differentially expressed genes ($p < 0.05$).

(F) A histogram showing relative m^6A peak enrichment of R-3A2A compared to R-WT mESCs, indicating higher m^6A methylation in pluripotency genes (PluriNetwork) for R-WT mESCs.

See also Figure S6, Table S3, Table S4, and Table S5.

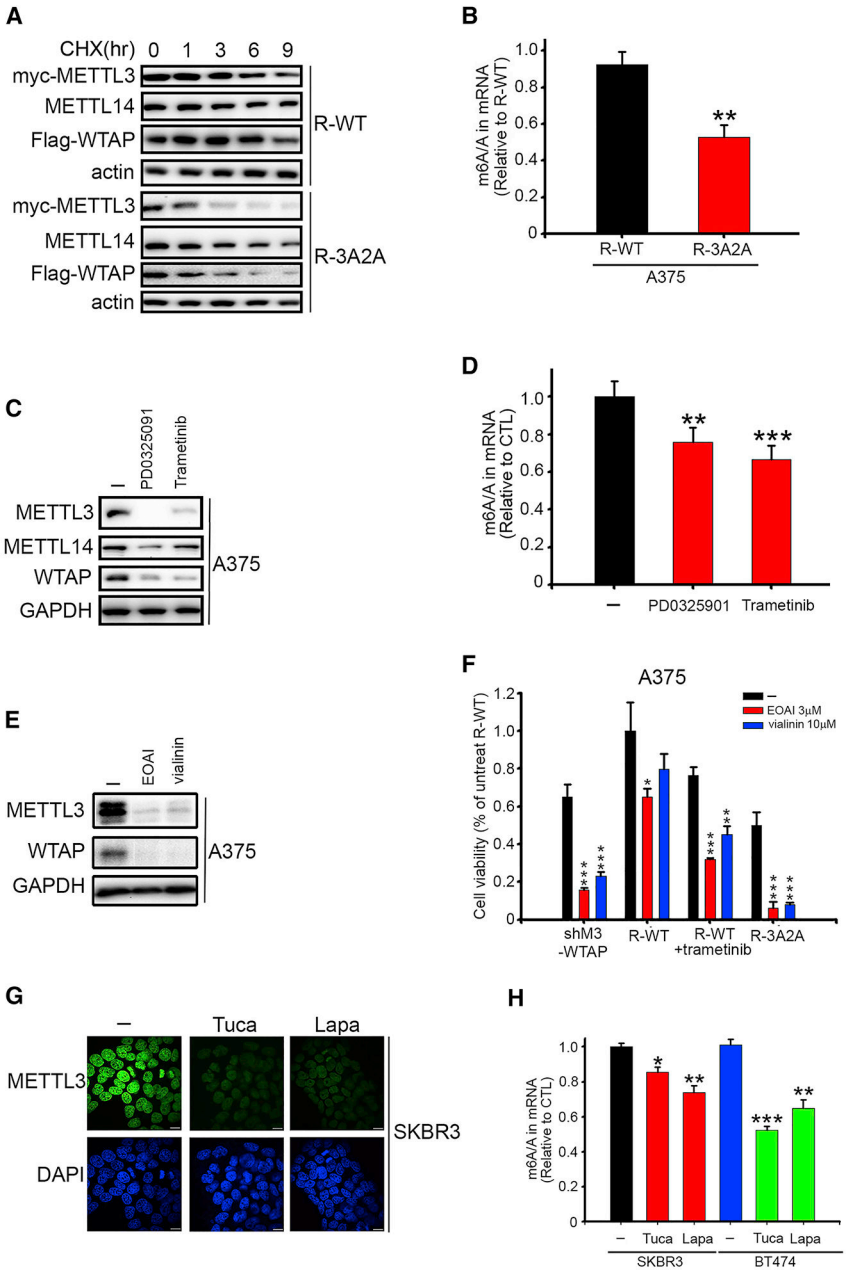

Figure 6. Phosphorylation of the m^{6}A Methyltransferase Complex May Affect Tumorigenesis

(A) Lysates of A375 stable transfectants harvested at different time points after treatment with cycloheximide (CHX) 10 μg/ml were analyzed by IB.

(B) LC-MS/MS quantification of the m^{6}A/A ratio in mRNA of A375 stable transfectants. **p < 0.01.

(C) After 8 hr treatment with 10 μM PD0325901 or 0.1 μM trametinib, lysates from A375 cells were analyzed by IB.

(D) LC-MS/MS quantification of the m^{6}A/A ratio in mRNA of A375 cells treated with 10 μM PD0325901 or 0.1 μM trametinib for 48 hr. **p < 0.01, ***p < 0.001.

(E) After 8 hr treatment with 10 μM EOAI3402143 (EOAI) or 30 μM vialinin A, cell lysates from A375 cells were analyzed by immunoblot.

(F) A375 stable transfectants as indicated were treated with 3 μM EOAI3402143 (EOAI) or 10 μM vialinin A before measuring cell viability by SRB assay. Data are presented as relative to the R-WT cells without drug treatment. *$p < 0.05$, **$p < 0.01$, ***$p < 0.001$.

(G) Immunofluorescence analysis of METTL3 (green) in SKBR3 cells treated with 1 μM tucatinib and 1 μM lapatinib for 8 hr. DAPI (blue) was used to mark the nucleus. Scale bars, 10 μm.

(H) LC-MS/MS quantification of the m^6A/A ratio in mRNA of SKBR3 and BT474 cells treated with 1 μM tucatinib and 1 μM lapatinib for 48 hr. *$p < 0.05$, **$p < 0.01$, ***$p < 0.001$.

Unless otherwise indicated, all data with error bars in this figure represent n = 3 replicates per group, and represent mean ± SEM. All p-values were also calculated by Student's *t* test. See also Figure S7.

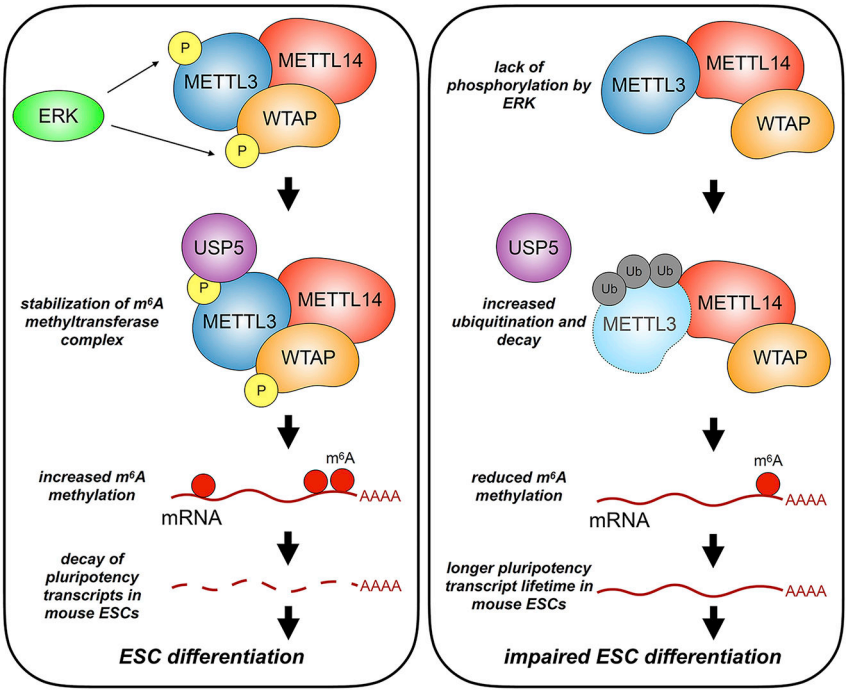

Figure 7.

A Schematic Model of the Role of the m^{6}A Methyltransferase Phosphorylation by ERK.

KEY RESOURCES TABLE

REAGENT or RESOURCE	SOURCE	IDENTIFIER
Antibodies		
Myc-tag (9B11) Mouse mAb	Cell Signaling	2276
Flag (M2) Mouse mAb	Sigma-Aldrich	F1804
HA-tag (C29F4) Rabbit mAb	Cell Signaling	3724
B-Raf (D9T6S) Rabbit mAb	Cell Signaling	14814
HER2/ErbB2 (D8F12) XP Rabbit mAb	Cell Signaling	4290
p-ERK1/2 (Thr202/Tyr204) (D13.14.4E) XP Rabbit mAb	Cell Signaling	4370
GAPDH (D16H11) XP Rabbit mAb	Cell Signaling	5174
β-Actin (8H10D10) Mouse mAb	Cell Signaling	3700
METTL3 (EPR18810) Rabbit mAb	Abcam	ab195352
p-METTL3 (S43)	Lifetein	customized
METTL14 (D8K8W) Rabbit mAb	Cell Signaling	51104
WTAP (4A10G9) Mouse mAb	Proteintech	60188
USP5 (EPR10454) Rabbit mAb	Abcam	Ab154170
IgG Isotype control (DA1E) Rabbit mAb	Cell signaling	3900
Necleolin (D4C7O) Rabbit mAb	Cell signaling	14574
ERK2 Rabbit Ab	Cell signaling	9108
ERK5 (D315V) Rabbit mAb	Cell signaling	12950
p38 (D13E1) Rabbit mAb	Cell signaling	8690
JNK2 (56G8) Rabbit mAb	Cell signaling	9258
Alexa 488- SSEA-1 (MC480) Mouse mAb	BioLegend	125609
Chemicals, Peptides, and Recombinant Proteins		
Phos-tag Acrylamide	Wako	AAL-107
cycloheximide	Sigma-Aldrich	01810
Actinomycin D	Sigma-Aldrich	A1410
MG-132	Sigma-Aldrich	474787
dabrafenib	Selleck Chemicals	S2807
PLX-4720	Selleck Chemicals	S1152
PD0325901	Selleck Chemicals	S1036
Trametinib	Selleck Chemicals	S2673
EOAI3402143	MedchemExpress	HY-111408
Vialinin A	Cayman Chemical	10010519
tucatinib	Selleck Chemicals	S8362
Lapatinib	Selleck Chemicals	S1028
SJB3–019A	MedchemExpress	HY-80012
SPOP-IN-6b	MedchemExpress	HY-122615
PD173074	Selleck Chemicals	S1264
DAPI	Sigma-Aldrich	D9542

REAGENT or RESOURCE	SOURCE	IDENTIFIER
Active ERK2	SignalChem	M28–10G
Active p38a	SignalChem	M39–10BG
Active ERK5	SignalChem	M32–10G
Active JNK2	SignalChem	M34–10BG
Active USP5	SignalChem	U505–380H
METTL3/METTL14	SignalChem	M323–380G
Nuclease P1 from Penicillium citrinum	Sigma-Aldrich	N8630
Calf Intestinal Alkaline Phosphatase	New England Biolabs	M0290
Mice FGF-4	R&D systems	5846-F4
Cumate	Sigma-Aldrich	268402
FastAP Thermosensitive Alkaline Phosphatase	Thermo Scientific	EF0654
Critical Commercial Assays		
Dynabeads mRNA DIRECT Kit	ThermoFisher	61006
EpiMark N6-Methyladenosine Enrichment Kit	New England Biolabs	E1610S
TruSeq Stranded mRNA Library Prep	Illumina	20020594
Luciferase Assay System	ProMega	E1500
PrimeScript RT Reagent Kit	Takara	RR037B
QuikChange Site-Directed Mutagenesis Kit	Strategene	200521
EpiQuik Histone H3 Modification Multiplex Assay Kit	Epigentek	P-3100–96
Deposited Data		
Mendeley dataset	This study	10.17632/nxgryg682r.1
CRISPR Screening, m^{6}A-MeRIP-seq, and RNA-seq	This study	GSE138776
Experimental Models: Cell Lines		
HeLa	American Type Culture Collection ATCC (ATCC)	CCL-2
293T	ATCC	CRL-3216
293TN	System Biosciences	LV900A-1
Mouse ESC METTL3KO	Provided by Howard Y. Chang	N/A
A375	Provided by Dr. Yu-Ying He	CRL-1619
CHL-1	ATCC	CRL-9446
MEL-624	Provided by Dr. Yu-Ying He	N/A
HCT116	ATCC	CCL-247
MCF7	ATCC	HTB-22
T47D	ATCC	HTB-133
SKBR3	ATCC	HTB-30
BT474	ATCC	HTB-20
Oligonucleotides		
For siRNAs, please see supplemental table S6	Qiagen	N/A
Recombinant DNA		
Circular RNA-GFP reporter	Provided by Z. Wang Laboratory	N/A

REAGENT or RESOURCE	SOURCE	IDENTIFIER
pCDH-CMV-MCS-EF1α-RFP	System Biosciences	CD512B-1
pCDH-CMV-circRNA-GGACT-EF1α-RFP	Generated in this study	N/A
pCDH-CMV- circRNA-GGTCT -EF1α-RFP	Generated in this study	N/A
CRISPR KO pooled library	Addgene	1000000048
Human METTL3	Addgene	53739
Human METTL14	Addgene	53740
Human WTAP	Addgene	53741
pKMyc	Addgene	19400
Human Flag-ATM	Addgene	31985
Human ATR	Addgene	31611
Human Flag-IKKε	Addgene	26201
Human HA-GSK-3β	Addgene	14754
Human ERK1	Addgene	23509
Human ERK2	Addgene	23498
Human B-Raf V600E	Addgene	17544
Human HA-Ubiquitin	Addgene	17608
Human Ubiquitin-KO	Addgene	17603
Human Ubiquitin-K6	Addgene	22900
Human Ubiquitin-K11	Addgene	22901
Human Ubiquitin-K27	Addgene	22902
Human Ubiquitin-K29	Addgene	22903
Human Ubiquitin-K33	Addgene	17603
Human Ubiquitin-K48	Addgene	16705
Human Ubiquitin-K63	Addgene	17606
pMD2.G	Addgene	12259
psPAX2	Addgene	12260
Human Flag-IKKα	Provided by M.C. Hung Laboratory	N/A
Human Flag-IKKβ	Provided by M.C. Hung Laboratory	N/A
Human HA-AKT	Provided by M.C. Hung Laboratory	N/A
Human Flag-mTOR	Provided by M.C. Hung Laboratory	N/A
Human HA-MEKDD	Provided by M.C. Hung Laboratory	N/A
Human HA-CDC2	Provided by M.C. Hung Laboratory	N/A
Human FAK	Provided by M.C. Hung Laboratory	N/A
Human EGFR	Provided by M.C. Hung Laboratory	N/A

REAGENT or RESOURCE	SOURCE	IDENTIFIER
Human HER2 V659E	Provided by M.C. Hung Laboratory	N/A
Human pCMV5-HA	Provided by M.C. Hung Laboratory	N/A
Human pCMV5-Flag	Provided by M.C. Hung Laboratory	N/A
pLightSwitch R01_3'UTR	Switchgear Genomics	S890001
pLightSwitch *NANOG*_3'UTR	Switchgear Genomics	S807466
Mouse METTL3	OriGene	MR209093
Mouse WTAP	OriGene	MR216877
Human USP5	OriGene	RC224191
Human pKMyc-METTL3	Generated in this study	N/A
Mouse pKMyc-METTL3	Generated in this study	N/A
Human pCMV5-HA-METTL14	Generated in this study	N/A
Human pCMV5-Flag-WTAP	Generated in this study	N/A
Mouse pCMV5-Flag-WTAP	Generated in this study	N/A
Human pCMV5-Flag-ERK1	Generated in this study	N/A
Human pCMV5-Flag-ERK2	Generated in this study	N/A
Human pCMV5-Flag-USP5	Generated in this study	N/A
Tet-pLKO-puro	Addgene	21915
Human Tet-On-shMETTL3	Generated in this study	N/A
Human Tet-On-shWTAP	Generated in this study	N/A
pCDH-CuO-MCS-EF1α-RFP	System Biosciences	QM512B-1
pCDG-EF1α-CymR-T2A-Neo	System Biosciences	QM400PA-2
pLenti-DsRed_IRES_SNCA:EGFP	Addgene	92195
Human pLenti-DsRed-IRES-METTL3-EGFP reporter	Generated in this study	N/A
Software and Algorithms		
FlowJo	Treestar	https://www.flowjo.com
RIGER	Broad Institute	https://software.broadinstitute.org/GENE-E/download.html
HISAT2	CCB JHU	https://ccb.jhu.edu/software/hisat2/index.shtml
DESeq2	Bioconductor	https://bioconductor.org/packages/release/bioc/html/DESeq2.html
exomePeak R	Bioconductor	https://bioconductor.org/packages/release/bioc/html/exomePeak.html
Guitar	Bioconductor	https://bioconductor.org/packages/release/bioc/html/Guitar.html

REAGENT or RESOURCE	SOURCE	IDENTIFIER
RADAR	GitHub	https://scottzijiezhang.github.io/RADARmanual/Mannual.htm
MeRIPtools	GitHub	https://scottzijiezhang.github.io/MeRIPtoolsManual/index.html
Homer	UCSD	http://homer.ucsd.edu/homer/motif/
Gene set enrichment analysis (GSEA)	Broad Institute	http://software.broadinstitute.org/gsea/index.jsp
GenePattern	N/A	https://cloud.genepattern.org/gp/pages/index.jsf